

# 14 Muon-trigger algorithms and performance

## 14.1 Introduction

In this chapter we present the main results on the expected physics performance of the muon-trigger system. A detailed simulation of the relevant detector components as well as the logic of the trigger has been made and is used to both optimize the system and confirm that the appropriate performance requirements, as outlined in Ref. [14-1], have been met.

The muon-trigger simulation is discussed (Section 14.2), and the analysis of the geometrical acceptance using this simulation reported (Section 14.3). The algorithms used by the trigger system to discriminate muon transverse momentum are introduced (Section 14.4) and the performance of the trigger analysed (Section 14.5). The trigger rates arising from known processes producing muons have been calculated (Section 14.6), as well as those from other particle fluxes present in the experimental hall (Section 14.7).

The discussion in this chapter closely follows that of [14-2], where a somewhat more detailed treatment of some topics can be found.

## 14.2 Simulation of the muon-trigger

In order to understand the performance of the ATLAS level-1 muon-trigger detailed simulations of both the ATLAS detector and trigger have been made. These include modelling of the passive material of the detector, of the active volumes and detector response of the muon-trigger counters, and detailed simulation of the hardware and logic of the muon-trigger itself. This has been done in the framework of the standard ATLAS simulation packages, using GEANT 321 [14-3] to describe the detector geometry in the DICE [14-4] program, and the ATRIG [14-5] package to simulate the trigger response.

### 14.2.1 Material of the detector and magnetic field

The material through which muons pass prior to traversing the trigger counters plays an important part in determining the acceptance of the trigger coincidence windows through the contribution of multiple scattering to the measured residual in the trigger chambers. The material in front of the trigger chambers is that of the end-cap and barrel toroids and the inner detector and calorimeters, both hadronic and electromagnetic. In both the barrel and the end-cap this material is dominated by the tile and liquid-argon calorimeters, as shown in Figure 14-1. Total material between the interaction point and the muon system constitutes between 10 and 15 absorption lengths, with somewhat more material in the region of the barrel-end-cap interface at  $|\eta| \sim 1.15$ . For lower momentum particles this material serves as a barrier between the interaction point and the trigger chamber planes; in the barrel, muons with  $p_T$  below 3 GeV are absorbed. All this material is included in the DICE simulation package. Material arising from cables, cooling components and other elements of the detectors that have yet to be finalized are not included in the simulation. These do however constitute an amount of material that can be neglected relative to that present in the current detector model.

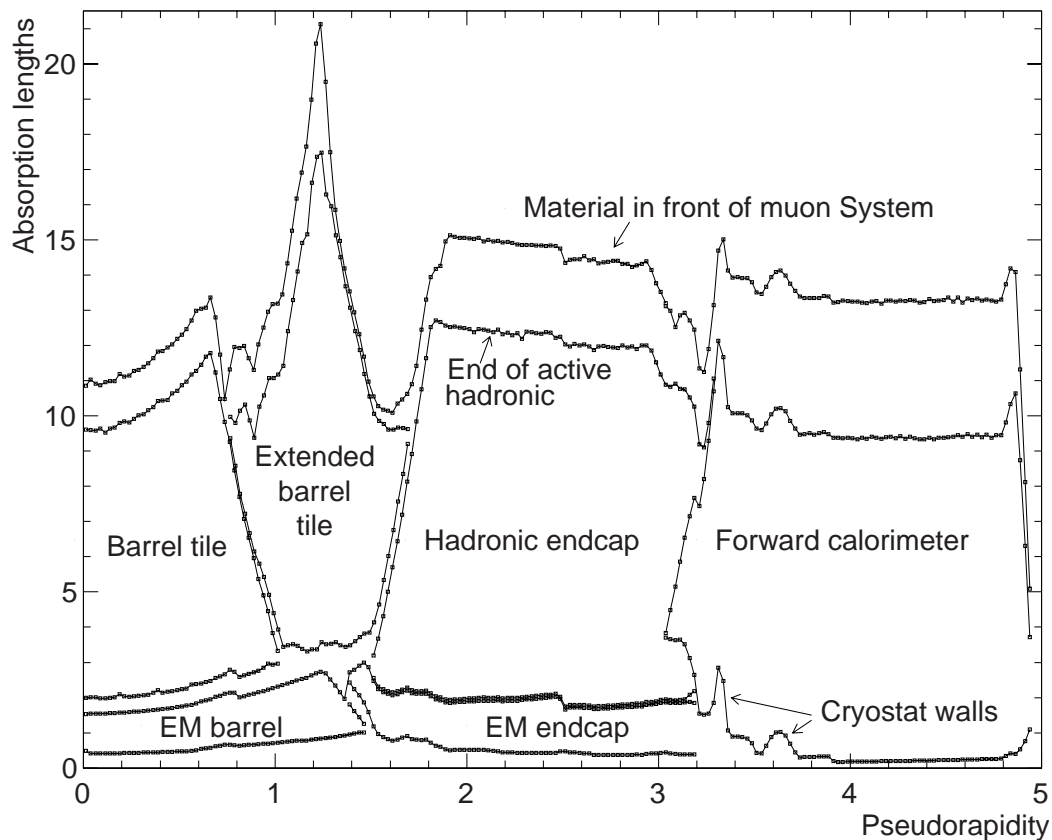


**Figure 14-1** Contributions of the various ATLAS detectors to the absorptive thickness shielding the muon system from primary collision products.

A precise map is made of the three-dimensional magnetic field arising from the barrel and end-cap toroids as well as the field of the central solenoid and hadron calorimeter which acts as the return yoke. This enables the path of charged particles in the simulation to be accurately tracked. The magnetic configuration used to calculate the field map is described in [14-6].

## 14.2.2 The trigger chambers

In the ATLAS detector simulation particular care has been taken in describing the different technologies of the muon spectrometer: monitored drift tubes (MDT), constituting the precision chamber system<sup>1</sup>, and resistive plate chambers (RPC) and thin gap chambers (TGC), forming the trigger system, are all simulated in detail with regard to the geometry and material composition. All detector units are divided into sensitive and non-sensitive regions. Layers of sensitive regions are interleaved with layers of passive material. The basic parameters and complete layout of all muon detectors are described in the ATLAS muon database [14-7]. A three-dimensional view of the simulated trigger system is shown in Figure 14-2 and a longitudinal view in Figure 14-3.

1. Cathode strip chambers (CSCs) provide the precision measurement of muon position and momentum for  $\eta > 2$ , in the first muon station. The CSCs are not modelled in the present simulation; MDT chambers have been simulated in their place.

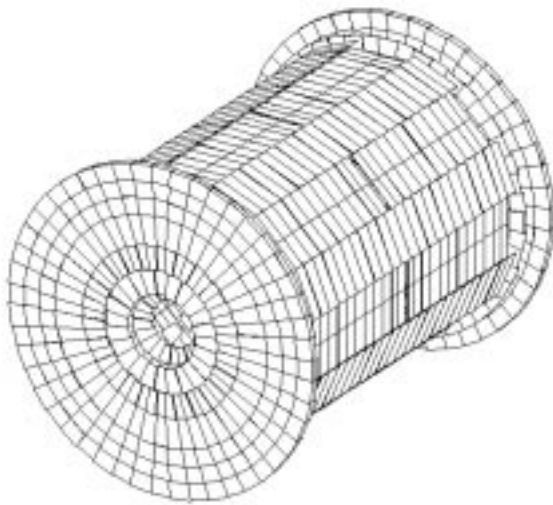


**Figure 14-2** Three-dimensional view of the simulated trigger system: resistive plate chambers (RPCs) in the barrel region, thin gap chambers (TGCs) in the end-cap region.

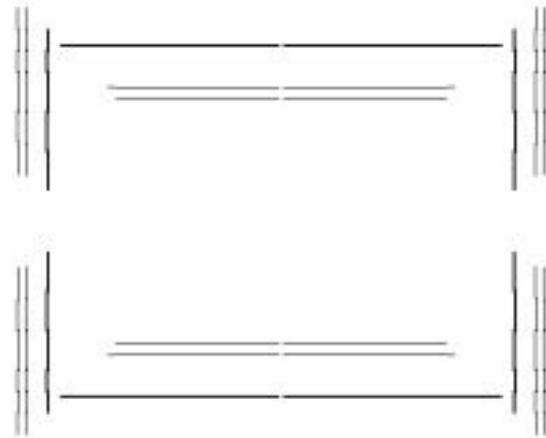


**Figure 14-3** Transverse view of the simulated trigger system with a longitudinal cut at  $\phi=0^\circ$ .

Trigger signals for the level-1 muon-trigger are provided by the trigger chambers: RPCs in the barrel and TGCs in the end-cap. In order to understand the many triggering issues raised by the performance of the trigger chambers these chambers have been modelled in detail within the DICE package. For the TGC a detector response is assumed such that hits are produced on only a single wire. In the RPC cluster size is modelled with an upper limit of two strips hit per track. Full hit efficiency for charged particles traversing active volumes is assumed in both subsystems. Within the active volumes spacers within the gas gaps are modelled. Effects that cause the chambers to deviate from their nominal geometry, such as temperature related effects and chamber displacement or deformation are not simulated.

This simulation has been used to optimize the design of the chamber geometry and the read out segmentation. It exactly reproduces the currently envisaged configuration of the chamber layout. This precise modelling allows the investigation of geometrical issues such as overlaps and acceptance holes which are crucial to the understanding of the trigger performance. For each subdetector in the simulation one layer of strips or one layer of wires is defined as a sensitive plane and digitization is modelled using the GEANT tracking of particles through the simulated detector volumes to determine the hit position.

### 14.2.3 Simulation of the trigger logic

The digits from the simulation of the trigger chambers are passed to a detailed simulation of the hardware containing the trigger logic. The full logic of the trigger, as well as the coincidence matrices in which coincidences are formed, is modelled. The details of the trigger electronics are discussed in Chapters 11 and 12, and the modelling of the logic in the simulation in Section 14.4.2.

The only significant aspects of the trigger that are not included in the simulation used for these performance studies are the timing information and some simulation of expected noise.

Dedicated GEANT simulations and numerical calculations have been performed to evaluate the effect on trigger rates and performance from these phenomena [14-8], [14-9].

## 14.3 Muon-trigger system acceptance

### 14.3.1 Introduction

In an apparatus as large and complex as the ATLAS muon spectrometer it is important to evaluate the effect of the geometrical acceptance on the trigger performance [14-10]. The analysis of the geometrical acceptance of the trigger system is based on the layout description available in the ATLAS muon database [14-7]. The layout of the trigger system, RPCs in the barrel and TGCs in the end-cap are shown in Figures 14-2 and 14-3.

### 14.3.2 Trigger chambers

The trigger system in ATLAS is composed of the RPC ( $|\eta| < 1.05$ ) and the TGC ( $1.05 < |\eta| < 2.4$ ) subsystems (Chapter 10). The acceptance of the low- $p_T$  trigger in the barrel system is defined by those tracks producing hits in at least three of the four inner trigger planes, and that of the high- $p_T$  trigger by those tracks within the low- $p_T$  acceptance and giving hits in at least one of the two planes of the outer station. For the TGCs the low- $p_T$  acceptance is defined by tracks with three from four possible hits in the outer two trigger stations (two doublet units); the high- $p_T$  trigger acceptance by tracks within the low- $p_T$  acceptance and having at least two hits in the three planes of the inner trigger station (triplet unit).

In Figure 14-4 the geometrical acceptance for very high- $p_T$  muons as a function of  $\eta$ , integrated over the azimuthal angle  $\phi$  is shown for both the low- and the high- $p_T$  configurations. This calculation considers only the geometry of the trigger system, and all generated tracks traversing the appropriate sensitive regions are considered to lie within the acceptance. No treatment of trigger coincidence windows is included in the analysis. The acceptance is limited by losses due to the presence of magnet and support structures (support feet of the inner detector and calorimeter and coil support ribs), and space allowed for services.

The acceptance as a function of  $\phi$ , averaged over  $\eta$ , in the range  $|\eta| < 2.4$ , is shown in Figure 14-5. The loss in acceptance due to the feet is seen in the two regions around 270 degrees, as well as the eight-fold modularity due to detector and magnet structure. Tracking very high- $p_T$  muons through the

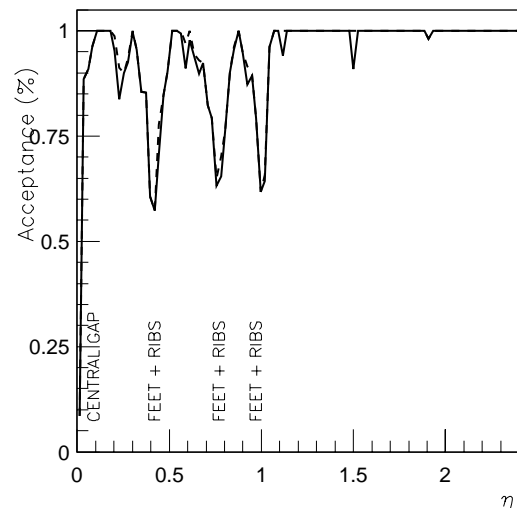


**Figure 14-4** Trigger acceptance integrated over  $\phi$  as a function of pseudorapidity for low- $p_T$  (dashed line) and high- $p_T$  (solid line) trigger settings. The acceptance loss at  $\eta=0$  can be seen as well as that due to support structures (feet and ribs).

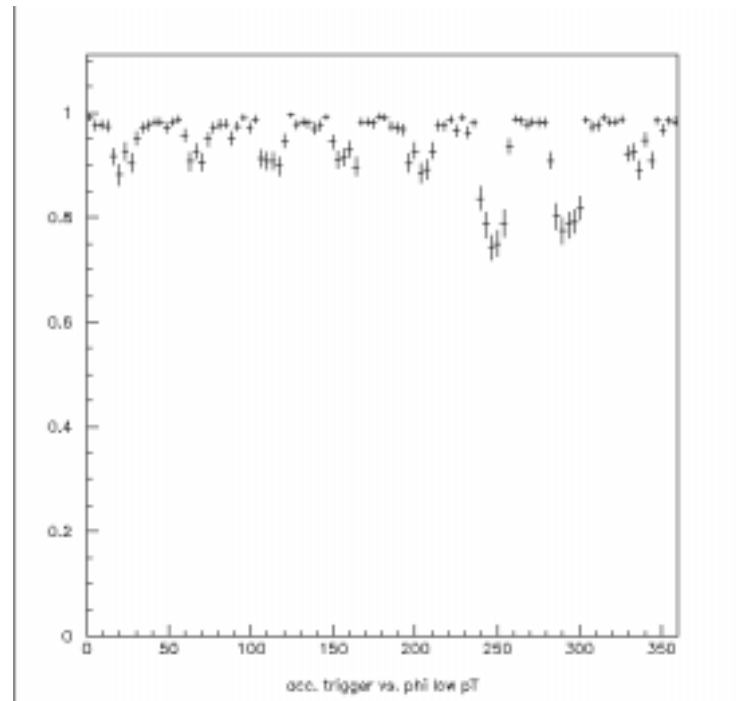


**Figure 14-5** Trigger acceptance as a function of  $\phi$ , averaged over  $\eta$ , in the range  $|\eta| < 2.4$ . The structures around  $270^\circ$  arise from the support feet and whilst the periodic acceptance loss is from the coil support ribs.

trigger system, the total acceptance loss in the region  $|\eta| < 2.4$  and integrated in azimuth is  $\sim 6\%$  for the low- $p_T$  coincidence, whilst for the high- $p_T$  coincidence the acceptance loss is  $\sim 6.5\%$ . The average acceptance of the muon-trigger system in the region ( $|\eta| < 2.4$ ) is shown in Table 14-1, normalized to the system coverage ( $|\eta| < 2.4$ ). In these calculations the contributions to the acceptance loss due to alignment corridors (which necessitate holes in the trigger counters) and holes in the TGCs for the displacement cables of the inner detector are neglected. The fraction of single muons that are double counted, considering only the geometrical overlap between the barrel and end-cap systems in the transition region, is  $\sim 0.77\%$  and  $\sim 0.15\%$  for the low- and high- $p_T$  coincidences respectively, within the trigger acceptance ( $|\eta| < 2.4$ ). It should be emphasized that logic exists in the MUCTPI (Chapter 13) to ensure that only a single level-1 trigger is given for such triggers; this calculation excludes the effect of such logic.

### 14.3.3 Transition region

At the transition between the barrel and the end-cap subsystems ( $|\eta| \sim 1.05$ ) a non-pointing gap, along the z-axis has been left, as can be seen in Figure 14-3. This allows permanent access to the barrel volume and for the passage of services. This region has been investigated to determine the level of acceptance loss and double-counting.

The trigger acceptance and the probability that single muons are identified in both subsystems in this region have been

**Table 14-1** Average acceptance of the Level-1 muon-trigger system, normalized to the region  $|\eta| < 2.4$ , (neglecting the alignment corridors and rail holes).

	barrel	end-cap	global system
low- $p_T$ trigger	0.909	0.976	0.940
high- $p_T$ trigger	0.885	0.974	0.935

investigated in the region  $0.8 < \eta < 1.2$  accounting for magnetic field and the material of the inner detectors. This shown in Table 14-2 for various  $p_T$  values.

**Table 14-2** Double counting as a fraction of acceptance in the region  $0.8 < \eta < 1.2$ , in %, in the trigger system for muons of 500, 20, 6 GeV  $p_T$ . The acceptance shown is for  $\mu^+$ , with the results for  $\mu^-$  in brackets. (The acceptance for  $\mu^+$  and  $\mu^-$  shown here is reversed for negative  $\eta$ .)

$(0.8 < \eta < 1.2)$	Double-counting rate		Acceptance	
	$p_T$ (GeV)	low- $p_T$ (%)	high- $p_T$ (%)	low- $p_T$ (%)
500	4.55 (4.2)	1. (1.)	93.1 (93.0)	92.3 (92.6)
20	8.2 (1.2)	3.2 (.3)	95.9 (90.2)	95.5 (89.0)
6	23.5 (0.)	6.9 (0.)	100.0 (77.0)	99.8 (78.2)

In the present layout an additional layer of RPCs has been added at the end of the barrel in the sectors covered by large chambers in such a way as to make the system as projective as possible in the bending plane. The additional chamber substantially increases the trigger acceptance in the region  $1.0 < |\eta| < 1.1$ , relative to the layout described in [14-6].

The present layout, used for all acceptance calculations here, does not include chambers around the coil support ribs. A modified layout has been investigated where very small chambers are added either side of each rib at  $\eta = 0.3, 0.7$  and  $1.0$  in all six small standard sectors. The dimension of these new chambers is about  $760 \times 300 \text{ mm}^2$  (active area) and their addition would result in an increase in acceptance of about 4%, normalized to the barrel  $\eta$  region  $|\eta| < 1.05$ .

### 14.3.4 Higgs to four muons: studies of the detector acceptance

Higgs boson decays to four muons are a benchmark process for muon detectors at the LHC. In order to evaluate in detail the effects of the muon-trigger system acceptance on the Higgs detection capabilities of ATLAS, we have tracked a sample of Standard Model Higgs decays to four muons ( $H \rightarrow ZZ^* \rightarrow 4\mu$ ) through the trigger detector simulation, for several values of the Higgs boson mass in the range 120–180 GeV. We have estimated that even for a dimuon-trigger more than 99% of the Higgs events generated within the trigger acceptance ( $|\eta| < 2.4$ ), for all generated Higgs masses, have two muons in regions covered by the trigger counters. Clearly the single muon-trigger will have an efficiency for triggering such events extremely close to 1. Details of the acceptance subject to demanding three or four detected muons are shown for a 140 GeV mass Higgs boson in Table 14-3.

**Table 14-3** Geometrical acceptance of the Level-1 muon-trigger for the process  $H \rightarrow ZZ^* \rightarrow 4\mu$ , for a 140 GeV mass Higgs boson. Acceptance is shown as a function of the number of muons lying within the trigger acceptance.

140 GeV Higgs mass	Low- $p_T$ acceptance	High- $p_T$ acceptance
Four muon detection	0.709	0.681
Three muon detection	0.963	0.955
Two muon detection	0.999	0.998

## 14.4 Track finding algorithms

### 14.4.1 Overview

The level-1 muon-trigger is based on the measurement of muon trajectories in two or three different planes (called stations). Muons are bent by the magnetic field generated by the toroids and their angle of deflection depends on their momentum, the field integral along their trajectory and the Coulomb scattering in the material lying in front of the trigger planes. The energy loss fluctuation is also important for low- $p_T$  transverse-momentum triggers.

The differences from the infinite momentum track, 'residuals', are measured using three trigger stations, Figure 14-6. The trigger plane farthest from the interaction point, in the end-cap, and

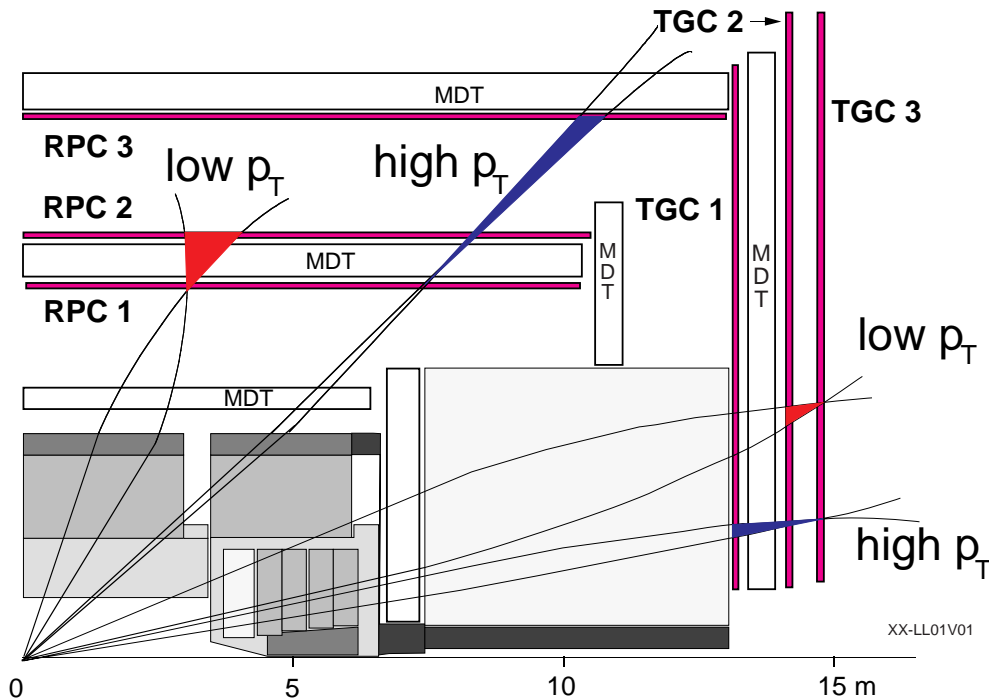


Figure 14-6 The level-1 muon-trigger scheme.

nearest to the interaction point in the barrel, is called the pivot plane and two different lever arms from the pivot to the other two trigger planes provide two different measurements of the residuals. The two different lever arms allow trigger thresholds to cover a wide range of momenta: the shorter lever arm (the pivot and station 2) covers a lower-momentum region and the longer one (the pivot and station 1 for the end-cap, the pivot and station 3 for the barrel), a higher-momentum region.

The residual distribution in a region  $(r, \phi)$  on the pivot plane reflects the momentum spectrum of muons passing through that region. The level-1 muon-trigger uses the residual distribution in order to discriminate muons with transverse momentum above some threshold from those below the threshold.

Each hit found in station RPC1 (TGC3) is extrapolated to station RPC2 (TGC2) along a straight line through the interaction point. A coincidence window is then defined around this point, where the window's size depends upon the required  $p_T$  threshold. The low- $p_T$  trigger condition is then satisfied if, for both projections

- there is at least one hit within the coincidence window
- at least one of the two low- $p_T$  stations has hits in both trigger planes, to satisfy the three-out-of-four majority logic.

The size of the coincidence window defines the  $p_T$  threshold applied in the trigger: the broader the window the lower the threshold.

A similar procedure is performed for the high- $p_T$  trigger, where the planes of RPC3 (TGC1) together with the pivot plane are used. The high- $p_T$  trigger is satisfied if

- the track passes the low- $p_T$  criteria, and
- in the barrel at least one hit in the two trigger planes of RPC3 are in coincidence, and in the end-cap if at least two of the three planes of TGC1 in the  $\eta$  view, and one of the two planes of TGC1 in the  $r$ - $\phi$  view, are within the appropriate coincidence window.

In the end-cap, read out segments (wire groups and strips) in the three trigger stations are aligned projectively so as to point to the nominal primary-vertex position. Wire groups in the three successive active layers of a triplet unit in station 1 are staggered by one third of their width relative to one another. Those in the two active layers of the doublet units of TGC2 and TGC3, and the strips in all stations, are staggered by half their width. This staggering makes effective position resolution one third or one half of the width of the actual read out segment.

In the barrel strip segments are similarly projective. Staggering is by approximately half a strip width in the central region of the detector ( $\eta < 0.6$ ) and by somewhat less in the higher  $\eta$  regions.

The muon-trigger is divided into regions in  $\eta$ - $\phi$  where independent thresholds can be set, i.e. where independent trigger windows can be used. This segmentation is discussed in Sections 11.1.2 and 12.3.

A time coincidence among hits is also required, to

- identify the bunch crossing,
- reduce the trigger rate from accidental coincidences induced by the cavern background.

The timing procedure of each of the two subsystems is described in Sections 11.2.4.1 and 12.4.6; the proposed procedure is equivalent to the setting of a time gate of 22 ns in the barrel and 31 ns in the end-cap, where logic exists to ensure that the appropriate bunch crossing is triggered.

#### 14.4.1.1 Declustering algorithm

Due to charge spread, cross talk or background, it is possible that a few neighbouring read out segments (wire groups or strips) may fire. Such hits can potentially produce multiple triggers. To reduce the combinatorial effect on the number of triggers, a declustering procedure is applied in both the barrel and end-cap trigger logic. In the barrel only the central hit (or two hits, in the case of an even number) is allowed to participate in the formation of trigger coincidences. The maximum multiplicity that can be handled is a system parameter; above that,

a certain number of hits will survive, depending on the reduction rules. In the end-cap, centre finding logic is implemented which selects only the second channel of sequential hits.

#### 14.4.2 Simulation of the trigger logic

The purpose of the trigger simulation is not only to evaluate the performance of the system, but also to optimize the trigger logic design. The trigger simulation should be flexible and duplicate in detail the hardware of the trigger logic in order to optimize parameters such as read out segmentation and the size of the coincidence matrices, as well as to debug the logic itself. This optimization is fed back to the design of the logic.

All the logic of the hardware of the trigger system is duplicated in the simulation of the trigger logic used for the performance studies of this document. All coincidences are performed using the appropriate granularity of the relevant trigger matrix and the rules and constraints on the allowed multiplicity in the logic at any single point are followed within the simulation. In the barrel, the staggering of the RPC strips and the declustering algorithm are not yet included in the simulation used here. No timing information is currently included in the simulation of either subsystem; this is not likely to impact significantly on the trigger performance since the timing has been optimized to include all hits from true prompt muon. Dedicated studies have been made to investigate this in both barrel and end-cap systems [14-8], [14-9].

### 14.5 Trigger coincidence windows and efficiency

#### 14.5.1 Transverse-momentum resolution

The coincidence windows of the level-1 muon-trigger are designed to offer momentum discrimination by including muons above threshold and excluding those below threshold which will be bent beyond the coincidence window. The  $p_T$  resolution at threshold in turn is a function of the trigger detector geometry (in particular the lever arm between stations 1 and 2, and station 3 – see Figures 11-1 and 12-1), the magnetic field intensity and its inhomogeneities, the Coulomb scattering in the central calorimeter and the width of the interaction region. Whilst this is mostly relevant to the primary bending direction ( $r$  or  $\eta$ ) there is also some bending in the orthogonal  $\phi$ -plane.

The trigger scheme is shown in Figure 14-6. In the barrel, where a muon is seen to leave a hit in both of the low- $p_T$  stations the projective extrapolation of the hit in station 1 (assuming an origin at the nominal p-p interaction point) to station 2 can be made assuming the muon path to be a straight line (i.e. the infinite momentum approximation). The distance between the extrapolated point in station 2 and the actual hit detected is defined as the separation parameter,  $d$ . In the end-cap system the low- $p_T$  trigger coincidence is made using station 3 (the pivot plane) and station 2.

The histograms in Figure 14-7 show as an example the value of the signed separation parameter  $d$ , for  $p_T=6\text{ GeV}$  muons, in a sector of the end-cap trigger chambers at  $\eta = 1.5$ . The two peaks shown in the histogram correspond to positive and negative muons. In the ideal case two narrow peaks are expected, approximately equidistant from and either side of  $d=0$ , one for each muon charge. In reality, the physics effects mentioned above introduce a significant smearing of these distributions and as a consequence the two peaks are broadened. This coincidence plot is a useful estimator of the  $p_T$  resolution at any trigger threshold relative to the bending seen in the trigger counters. The method followed consists of fitting each peak with a Gaussian function with parameters  $\sigma$  and  $\mu$ ; the parameter  $\mu$  is the average value of  $d$  (for a given muon charge) and is proportional to  $1/(p_T-p_{T0})$  (where  $p_{T0}$  is the average  $p_T$  lost in traversing the calorimeter), while  $\sigma$ , the width of the Gaussian, represents the physics limitations on the measurement of  $d$ . Therefore the ratio  $\sigma/\mu$  is a measure of the transverse-momentum resolution, whilst  $\mu$  quantifies the amount of bending. In order to evaluate the contribution of each source of smearing, the parameter  $d$  has been plotted with the relevant physics effects introduced into the simulation one at a time.

Throughout the barrel detector Coulomb scattering is the most important physics effect limiting the precision of the  $p_T$  measurement for the low- $p_T$ , although its effects are somewhat  $\eta$ - and  $\phi$ -dependent. The typical resolution figure is 30%, rather uniform throughout the  $\eta$ - $\phi$  space covered.

Figures 14-7 and 14-8 show the coincidence plot for 6 GeV  $p_T$  muons in the end-cap system; the typical momentum-resolution figure is about 10% where this is mainly limited by the Coulomb scattering in the calorimeter. However, there are  $\phi$  regions in the  $\eta$  interval  $1.0 < |\eta| < 1.8$  where this resolution is significantly worse. This effect is due to the combination of the magnetic fields produced by the barrel and end-cap toroid coils. Since in these regions the field integral is low, the associated  $d$  parameter is low, and the resulting muon momentum resolution  $\delta p_T/p_T = \sigma/\mu$  is worse than elsewhere.

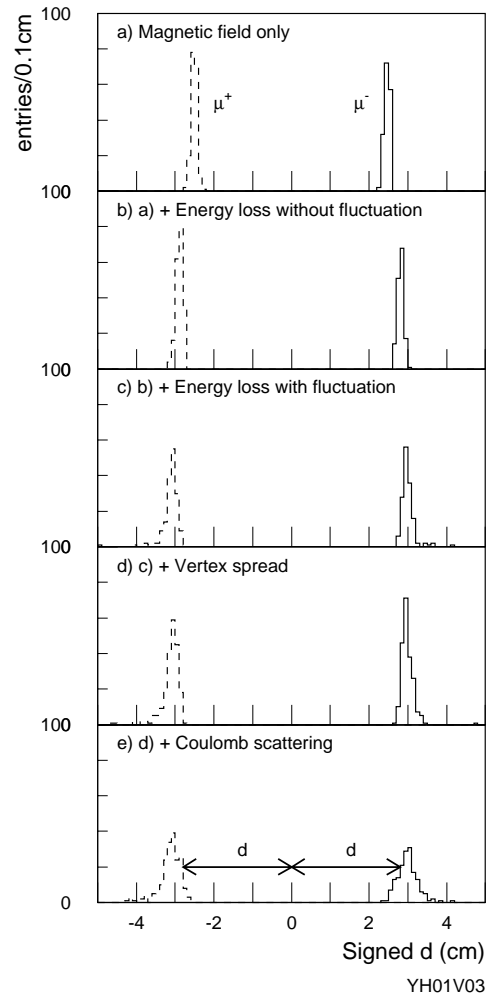


**Figure 14-7** Coincidence plot for 6 GeV  $p_T$  muons, both charges, generated in the end-cap close to  $\eta = 1.5$ ,  $\phi = 0.0-2.0^\circ$ . Several histograms are shown in the same picture, representing: a) magnetic field only, (no vertex spread, Coulomb scattering, energy losses or detector response); b) as a) + energy loss without fluctuations; c) as a) + energy loss with fluctuations; d) as c) + vertex spread; e) as d) + Coulomb scattering. The detector granularity is not considered in this plot.

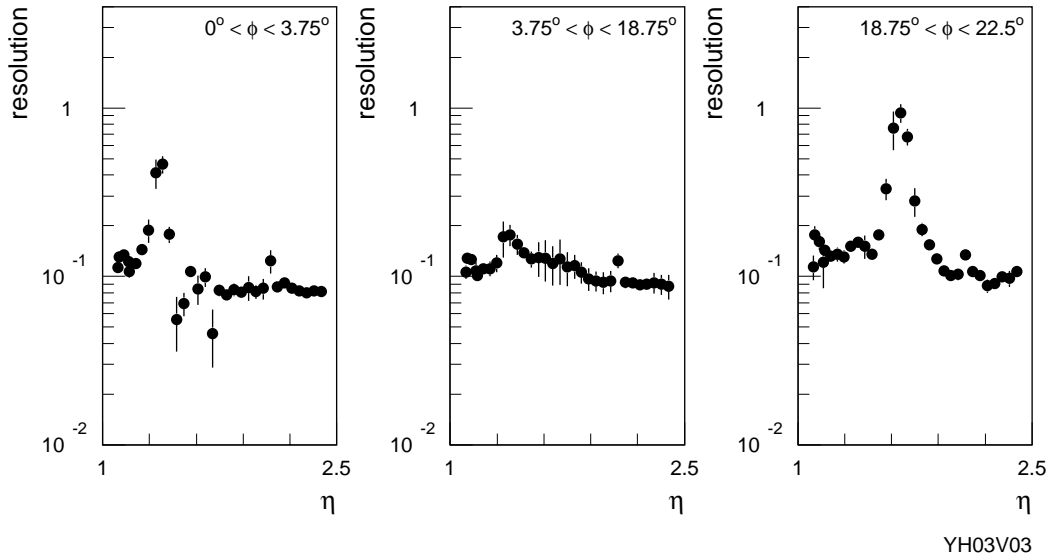


**Figure 14-8** Transverse-momentum resolution,  $\delta p_T/p_T$ , of the end-cap system for 6 GeV  $p_T$  muons as a function of  $\eta$  and  $\phi$ .

This is shown in Figure 14-9 (showing data in the region  $\eta = 1.3$ ,  $\phi = 0.0^\circ$ – $2.0^\circ$ ) where the two opposite-sign muon peaks are almost overlapped. The result of this is that almost all  $p_T$  discrimination in such regions is lost.

As shown in Figure 14-10 these poor-resolution regions are located along the barrel and end-cap coils, with  $\eta$  values of  $\sim 1.3$  ( $\phi$  coordinates of the end-cap coils) and  $\sim 1.6$  ( $\phi$  coordinates of the barrel coils). Figure 14-8 shows the  $p_T$  resolution in the end-cap as a function of  $\eta$  and  $\phi$ , for three different  $\phi$  regions across the whole  $\eta$  range of the end-cap acceptance. In the barrel there are no such overlapping fields, and as such the resolution is rather constant across both  $\eta$  and  $\phi$ .

For the high- $p_T$  trigger the  $p_T$  estimation is made using hits in station 1 (station 3) and station 3 (station 1) in the barrel (end-cap) system. The trigger scheme adopted also uses the coincidence in station 2 for track confirmation; this is to reduce the trigger rate from fake muons, rather than to offer any improvement in the momentum discrimination of the trigger. Here the resolution is limited mainly by the Coulomb scattering and the width of the interaction region ( $\sigma_{vtx} \sim 5.5$  cm). At  $p_T = 20$  GeV the transverse-momentum resolution is  $dp_T/p_T \sim 0.40$  in the barrel and  $dp_T/p_T \sim 0.15$  in the end-cap. The higher performance of the end-cap system is largely due to the higher field integral provided by the forward toroids [14-6] and the different trigger counter layout that allows the end-cap trigger system to make full use of the available field integral; indeed, the barrel trigger counters are placed inside the magnet, while the end-cap trigger system is located

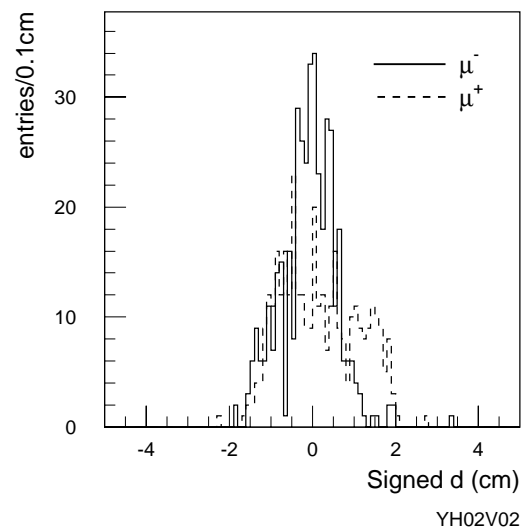


**Figure 14-9** Coincidence plot for 6 GeV  $p_T$  muons, for both charges, generated at  $\eta = 1.3$ ,  $\phi = 0.0^\circ$ – $2.0^\circ$ . The two charged-muon peaks are overlapping each other almost completely, demonstrating the loss of almost all  $p_T$  discrimination.

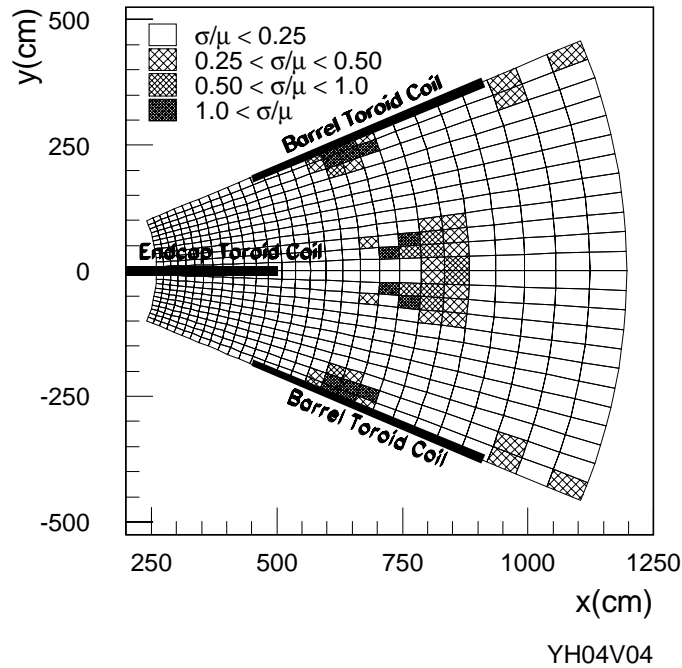


**Figure 14-10** Position of the regions in the end-cap system where momentum resolution is poor. A single octant is shown where the subdivisions represent trigger sub-sectors, and the dark lines show the position of the barrel and end-cap toroid coils.

beyond the toroids. The high- $p_T$  trigger in the end-cap system shows the presence of the same low field-integral regions as seen for low- $p_T$  muons.

Plots of the  $d$  parameter are used to determine the coincidence windows for high- and low- $p_T$  trigger thresholds. The resolution plot is used to identify regions where the  $p_T$  discrimination of the trigger system is poor.

### 14.5.2 Coincidence windows

The sizes of the trigger windows that determine the  $p_T$  threshold have been computed for the proposed trigger system by tracking single muons through the ATLAS detector using Monte Carlo simulation techniques (see Section 14.2). The size of a coincidence window is defined such that 90% of the muons of each charge within the detector acceptance, generated with transverse momentum equal to the threshold, are accepted. The absolute normalization is determined by the trigger efficiency for muons with momentum far above the threshold, and corresponds to the geometrical acceptance of the trigger detector.

The coincidence windows of the trigger will ultimately be defined as areas in two dimensions on the surface defined by inputs to the coincidence matrix in the two projections  $\eta$  and  $\phi$ . The boundaries of the window for any one trigger threshold will be determined using simulated muons, and once data have been collected using true muons in ATLAS. The studies made here have approximated the two-dimensional trigger window to a simple rectangle. This model reproduces exactly the barrel coincidence logic and represents a good approximation to the end-cap trigger coincidence logic.

As discussed in Section 14.5, the window size depends on the trigger-counter geometry, the magnetic-field intensity, the Coulomb scattering and the energy-loss fluctuation in the central calorimeter, and the width of the interaction region ( $\sigma_{\text{vtx}} \sim 5.5$  cm). The detector granularity also contributes to the momentum resolution; it has been designed by optimizing the opposing requirements of trigger performance and number of trigger channels. Since the geometry and the large variations in both granularity and field strength in the end-cap make this region more complex these studies have concentrated on that subsystem.

The sizes of coincidence windows for the 6 GeV low- $p_T$  threshold in the barrel are shown in Figure 14-11 for standard sectors. Since the position of trigger stations of the special small

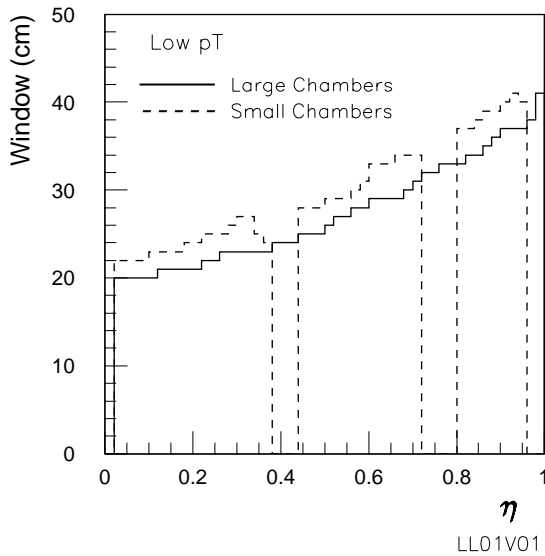


**Figure 14-11** Window size in the barrel as a function of  $\eta$  in both the small and large chambers, for 6 GeV muons in the bending plane of the low- $p_T$  system.

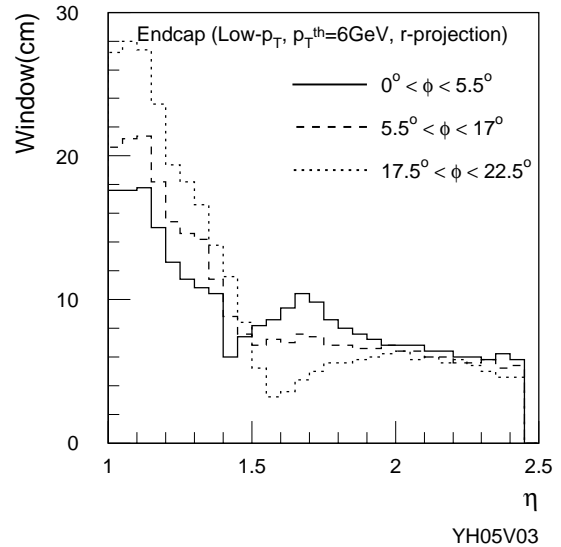


**Figure 14-12** Window size in the end-cap as a function of  $\eta$  and  $\phi$  for 6 GeV muons in the bending plane of the low- $p_T$  system. Three  $\phi$  intervals are considered: the end-cap toroid region ( $0^\circ$  to  $5.5^\circ$ ), the barrel toroid region ( $17^\circ$  to  $22.5^\circ$ ), and the region between the two ( $5.5^\circ$  to  $17^\circ$ ).

chamber sectors is the same as the standard small sectors (they differ only in that the coverage along the beam-line direction is reduced), the coincidence-window size is the same so long as muons cross both trigger stations of the low- $p_T$  system.

In the end-cap low- $p_T$  system the coincidence windows show a pronounced  $\phi$ -dependence. This is due to the complex magnetic fields produced by the combination of the barrel and end-cap toroid coils. Neighbouring  $\eta$ - $\phi$  regions are seen with significantly different field integrals, and this has a direct impact on the size of the coincidence windows.

Figure 14-12 shows the size of the coincidence window, in the  $\eta$  projection, in the end-cap as a function of  $\eta$  and  $\phi$ , for a threshold of 6 GeV  $p_T$  in the low- $p_T$  trigger system. These are optimal window sizes calculated independently of the actual detector granularity. The  $\eta$  and  $\phi$  values are those of the track position on the pivot plane.

The coincidence window is not symmetric around the extrapolated point of the infinite momentum path: Muons of a given charge, bending towards high  $|z|$  regions (in the barrel) or high  $r$  regions (end-cap), cross station 2 at a distance from the extrapolated point larger than that for muons of opposite charge. This effect increases with  $|\eta|$  in the barrel and with  $r$  in the end-cap. This leads to asymmetric coincidence windows, formed by independent left and right half-windows. The difference between the right and left half-window is 7/10 cm in the large/small chambers at  $|\eta| \sim 0.9$  in the barrel and 3.5 cm at  $|\eta|$  close to 1 in the end-cap. The size of each half-window is evaluated accounting for the relative trigger efficiency of positive and negative muons independently, to minimize possible effects on charge-asymmetry measurements.

The coincidence window for 6 GeV transverse-momentum thresholds in the  $r$ - $\phi$  projection is shown in Figure 14-13 for the end-cap; in this case the window is defined such that

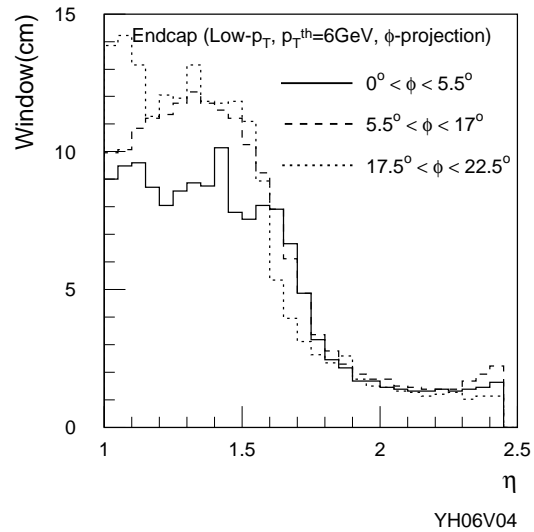


**Figure 14-13** Window size in the end-cap for 6 GeV muons in the low- $p_T$  system,  $r$ - $\phi$  projection as a function of  $\eta$  and  $\phi$ . Three  $\phi$  intervals are considered: the end-cap coil region ( $0^\circ$  to  $5.5^\circ$ ), the barrel coil region ( $17^\circ$  to  $22.5^\circ$ ) and the region between the two ( $5.5^\circ$  to  $17^\circ$ ).

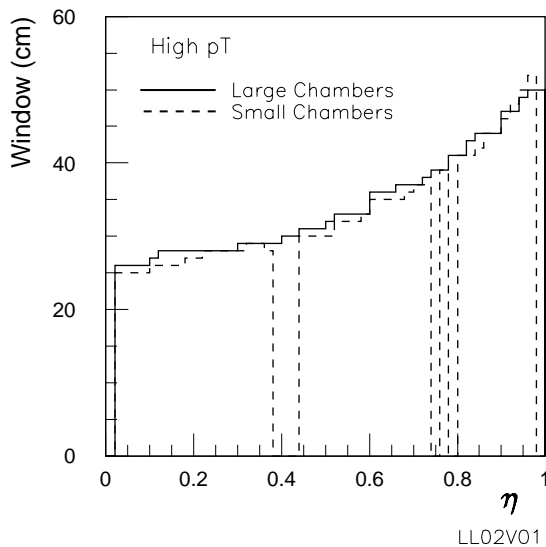


**Figure 14-14** Window size in the barrel system as a function  $\eta$  in both the small and large chambers, for 20 GeV muons in the  $\eta$  projection.

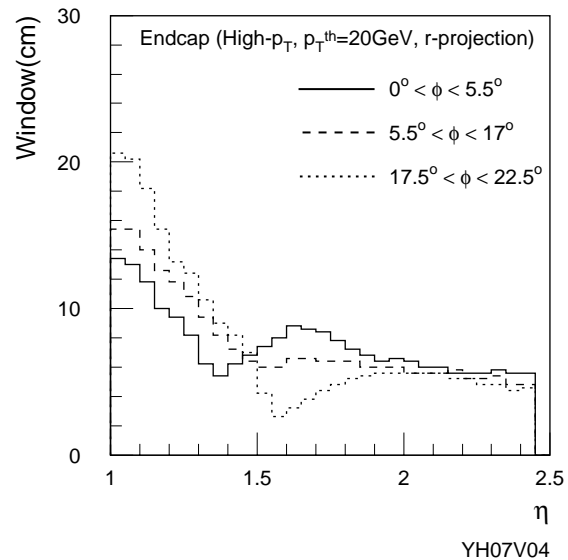


**Figure 14-15** Window size as a function of  $\eta$  and  $\phi$  for 20 GeV  $p_T$  muons in the  $\eta$  projection end-cap high- $p_T$  system. Three  $\phi$  intervals are considered: the end-cap coil region ( $0^\circ$  to  $5.5^\circ$ ), the barrel coil region ( $17^\circ$  to  $22.5^\circ$ ) and the region between the two ( $5.5^\circ$  to  $17^\circ$ ).

more than 99% of the muons within the geometrical acceptance are accepted. The coincidence in the  $r$ - $\phi$  plane serves to reduce the fake muon-trigger rate induced by the cavern background. In

the final windowing scheme both  $\eta$  and  $r$ - $\phi$  windows will be applied simultaneously in a true two-dimensional window. In Figure 14-13 it is possible to see the effect of the non-toroidal field in the transition region: In this region, muons also bend in the  $r$ - $\phi$  view, whereas, in an ideal toroidal system, only the Coulomb scattering in the calorimeter and the field in the central solenoid would be expected to produce deviation from the original muon trajectory.

A similar analysis has been performed for the nominal high- $p_T$  threshold,  $p_T^{\text{th}} = 20$  GeV. Figure 14-14 shows the size of this coincidence window, in the  $\eta$  projection, for the barrel, and Figure 14-15 shows the same projection for the end-cap. The same coincidence in the other projection is shown in Figure 14-16 for the end-cap. Here also the  $\phi$ -dependence of the trigger window size in the end-cap system is visible. For the  $r$ - $\phi$  view, the coincidence window is again defined such that more than 99% of the muons with  $p_T^{\text{th}} = p_T^{\text{th}}$  are accepted.

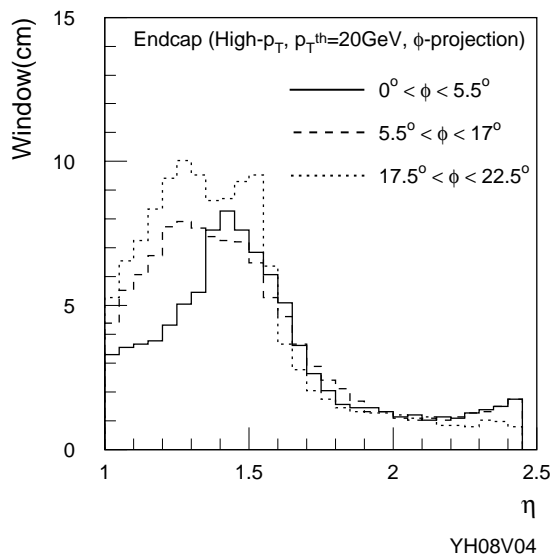


**Figure 14-16** Window size in the end-cap as a function of  $\eta$  and  $\phi$  for 20 GeV muons in the high- $p_T$  system,  $r$ - $\phi$  projection. Three  $\phi$  intervals are considered: the end-cap coil region ( $0^\circ$  to  $5.5^\circ$ ), the barrel coil region ( $17^\circ$  to  $22.5^\circ$ ) and the region between the two ( $5.5^\circ$  to  $17^\circ$ ).

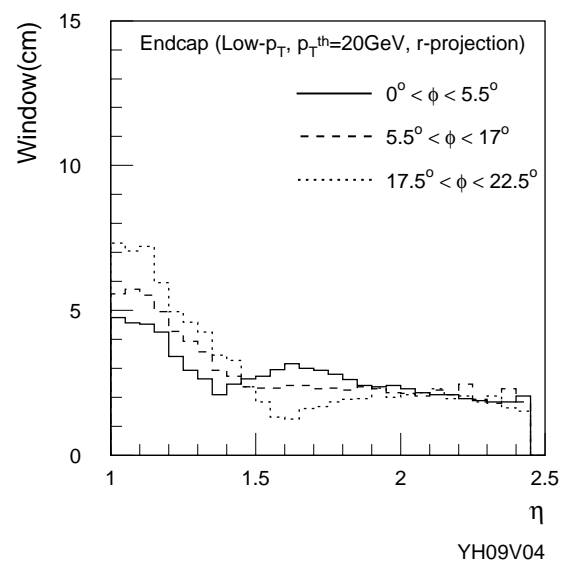


**Figure 14-17** Window size in the end-cap as a function of  $\eta$  and  $\phi$  for 20 GeV muons in the low- $p_T$  system, bending projection. Three  $\phi$  intervals are considered: the end-cap coil region ( $0^\circ$  to  $5.5^\circ$ ), the barrel coil region ( $17^\circ$  to  $22.5^\circ$ ) and the region between the two ( $5.5^\circ$  to  $17^\circ$ ).

Figure 14-17 shows the size of the window in the  $\eta$  projection for 20 GeV  $p_T$  muons in the low- $p_T$  end-cap system. The window is approximately a factor of five smaller than that for 6 GeV muons, reducing significantly therefore the random trigger rate. The evaluation of the coincidence window size and the intrinsic momentum resolution has a direct impact on the optimization of the trigger detector granularity, largely with regard to the primary bending projection. The detector pitch should be fine enough that no significant deterioration of the intrinsic resolution is introduced by the system, and yet cost constraints favour a coarser pitch and fewer channels. In the barrel, the typical window size is around 35 cm, both for low and high- $p_T$  threshold, with an intrinsic momentum resolution of about 40% at low- $p_T$  threshold and about 15% for the high- $p_T$  threshold. A read out pitch of the order of 3–4 cm, as proposed in this document, is adequate to maintain the physics performance of the system. Conversely, for the end-cap system the coincidence window can be as small as 6 cm, with an intrinsic resolution of 10% at low- $p_T$  threshold and about 15% for the high- $p_T$  threshold. A wire-group size of about 14 (21) mm for the doublet (triplet) TGC stations, corresponding to an effective read out pitch of

7mm (from the effective resolution of half a wire-group, see Section 14.4), introduces an additional small smearing effect, reducing the resolution slightly, but still quite adequate for the trigger.

The detector granularity in the other projection is less crucial for the trigger performance and it has been optimized to provide an accurate second coordinate track measurement for muon reconstruction.

### 14.5.3 Trigger efficiency and masking

In order to evaluate the level of rejection of muons below any one trigger threshold by the trigger system, single muons over a wide range of momenta have been generated and passed through the ATLAS detector and trigger simulation. The barrel and end-cap systems have been studied independently, and the trigger efficiency evaluated as a function of  $p_T$ . In the end-cap where the window size and the trigger efficiency have a strong  $\eta$  dependence, the efficiency has been evaluated as a function of  $\eta$  (integrating over  $\phi$ ). These calculations are performed in a fiducial rapidity range within the geometrical acceptance of each system.

The trigger efficiency has been evaluated by simulating the trigger logic using coincidence windows defined as explained in the previous section. The efficiency is given simply by the ratio of the number of triggered muons to the number generated within the  $\eta$  fiducial interval, including also geometrical acceptance effects. The trigger efficiency is plotted in Figures 14-18 and 14-19 for the 6 GeV  $p_T$  threshold in the low- $p_T$  system, for both muon charges, as a function of  $p_T$ , for the barrel and end-cap.

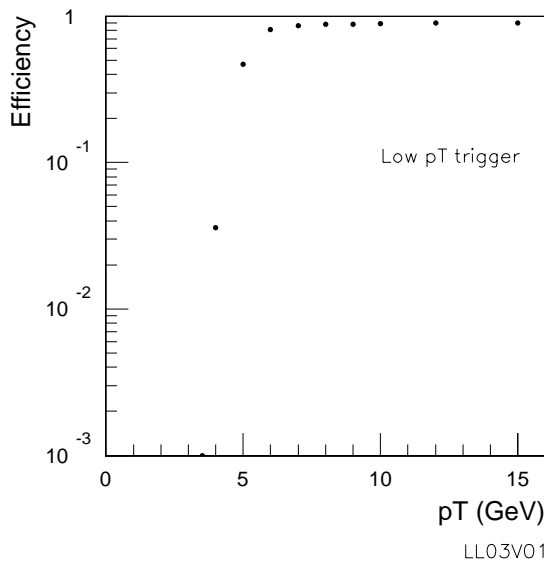


**Figure 14-18** Trigger efficiency for the barrel for the 6 GeV threshold in the low- $p_T$  system.

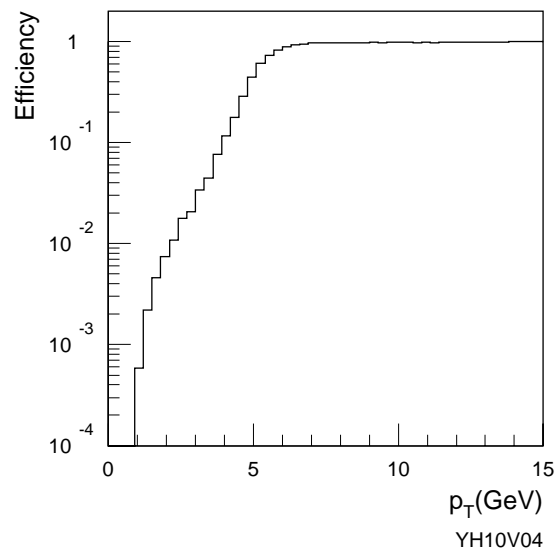


**Figure 14-19** Trigger efficiency for the end-cap for the 6 GeV threshold in the low- $p_T$  system.

Figure 14-20 shows the trigger-efficiency curve for  $\eta$  around 1.3 in the low- $p_T$  end-cap system as a function of  $\phi$ . It can be seen that the discrimination of the trigger in the  $\phi$  interval with poor resolution is weaker than for other  $\phi$  values. This is the consequence of the regions with low field integral, as discussed in Section 14.5.1.

The trigger efficiency for low- $p_T$  ( $<6\text{ GeV}$ ) muons in the barrel is lower than in the end-cap since in the barrel the central calorimeter acts as a barrier to muons with  $p_T < 3.0\text{ GeV}$ ; this threshold being the average energy loss for a muon that traverses the calorimeter at normal incidence. In the end-cap the calorimeter geometry differs and the energy absorption sets a limit on  $p$  rather than  $p_T$ :  $p_T > E_{\text{loss}} \times \sin\theta$ , where  $E_{\text{loss}}$  is about  $4\text{ GeV}$  and  $\sin\theta$  can be as small as  $0.17$ , thus bringing the calorimeter threshold below  $1\text{ GeV}$ .

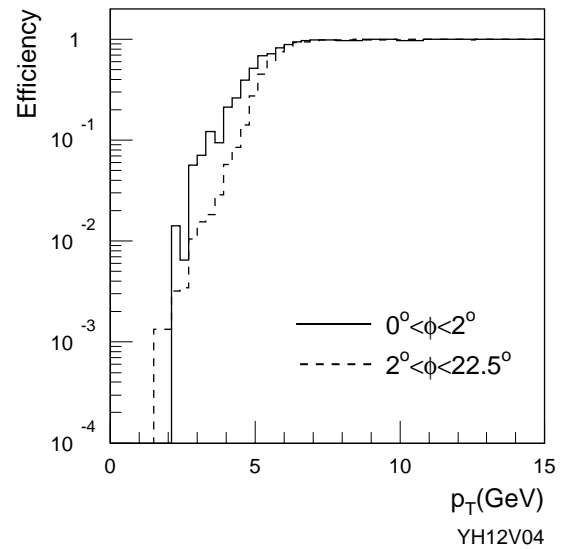


**Figure 14-20** Trigger-efficiency curve for  $6\text{ GeV}$  threshold in the end-cap low- $p_T$  system, for muons generated with  $\eta$  around 1.3 for a)  $\phi = 0\text{--}2^\circ$ ; b)  $\phi = 2\text{--}22.5^\circ$

The level of precision of the calculation of trigger efficiency at very low  $p_T$  ( $p_T < 2\text{ GeV}$ ) is of particular importance for the estimation of the trigger rate induced by muons from in-flight decays of light mesons. The cross-section for this process is large and very steeply rising with decreasing  $p_T$  around  $p_T = 2\text{ GeV}$  (see Section 14.6.1.1). This aspect is of particular importance for the end-cap system, where low- $p_T$  muons are not naturally removed by the material of the central calorimeter. The present statistical error on the efficiency at low- $p_T$  is about  $15\%$ . Efforts have been made to cross-check both the simulation of the trigger and the mechanics of the efficiency calculation. An entirely independent implementation of the simulation of the end-cap trigger chamber geometry and trigger logic has been made and the efficiency calculations presented here duplicated. It is seen that the independent calculation reproduces overall efficiencies presented here, including those regions where most rate is seen ( $p_T < 2\text{ GeV}$ ), at the  $10\%$  level. This suggests that systematic errors on the efficiencies arising from coding and simulation uncertainties are at or below this level.

Efficiency curves, as a function of  $p_T$  are shown in Figures 14-21 and 14-22 for  $p_T^{\text{th}} = 20\text{ GeV}$  in the high- $p_T$  system for the barrel and end-cap.

For both low- and high- $p_T$  trigger thresholds, triggered muons with generated momentum below threshold have been studied in detail in order to verify the performance of the simulated trigger logic. These studies have focused on the end-cap system since here the trigger performance is more sensitive to the complex magnetic field in the forward region than to the more uniform field in the barrel.

Figure 14-23 shows hit positions in the pivot plane of the low- $p_T$  end-cap trigger system (station 3) for triggered muons with  $p_T$  in the range  $1$  to  $5\text{ GeV}$  where the threshold value was  $6\text{ GeV}$ . A significant fraction of triggered muons below threshold are concentrated in those  $\eta$ - $\phi$  regions where the  $p_T$  resolution is poor, see Figure 14-10. However these regions get more diffuse for lower- $p_T$  muons.

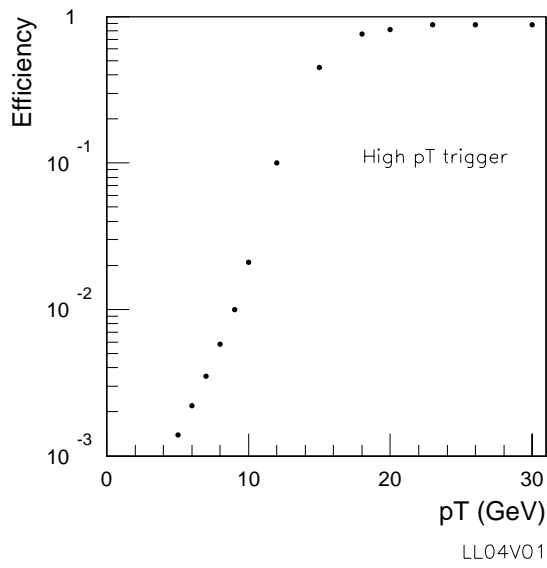


**Figure 14-21** Trigger efficiency for the barrel system as a function of  $p_T$ , for the 20 GeV high- $p_T$  threshold.

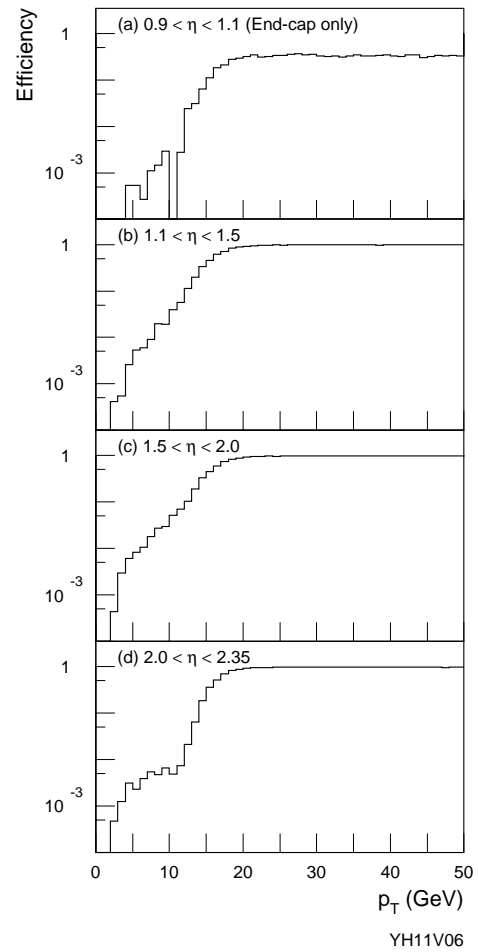
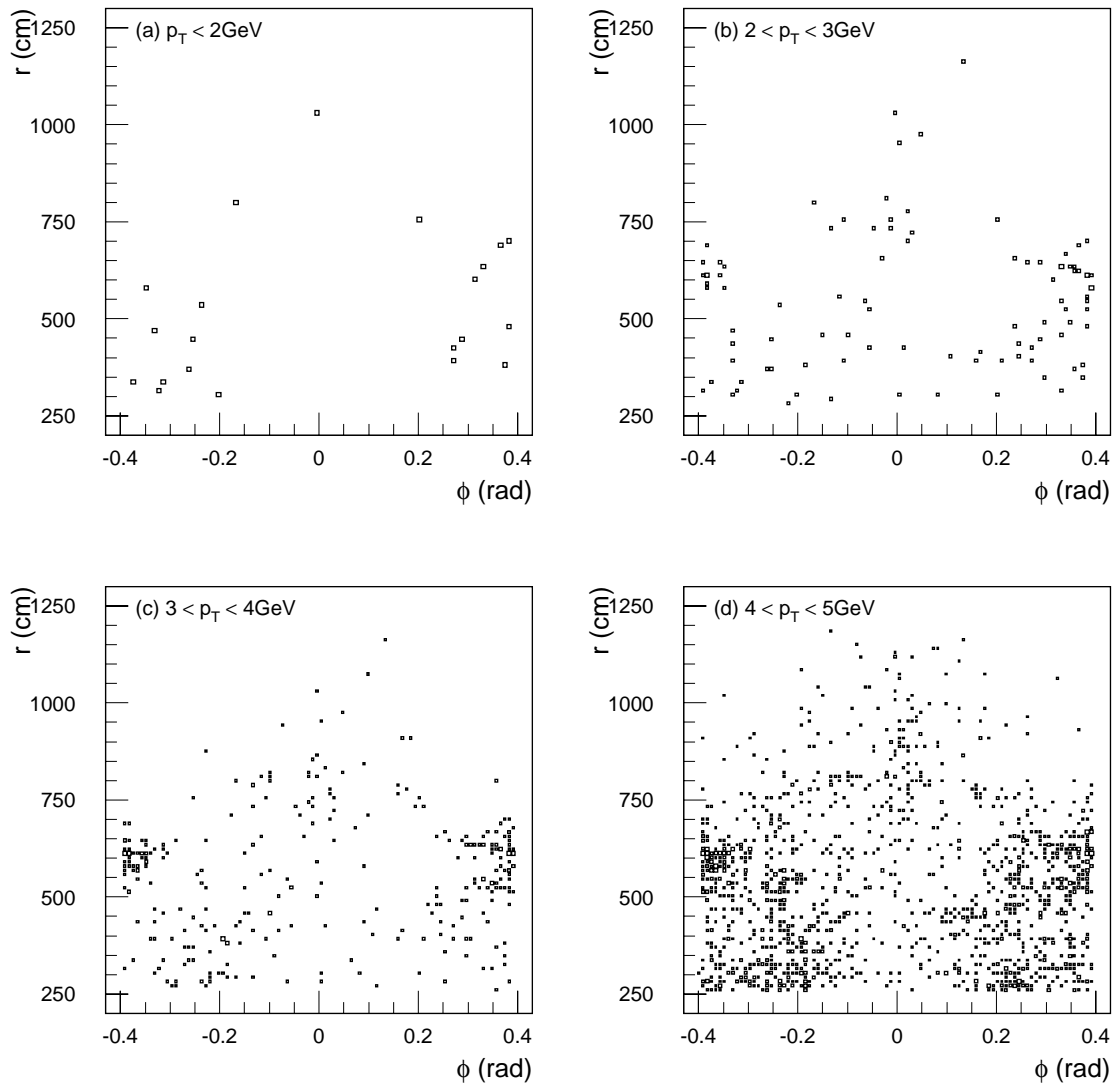


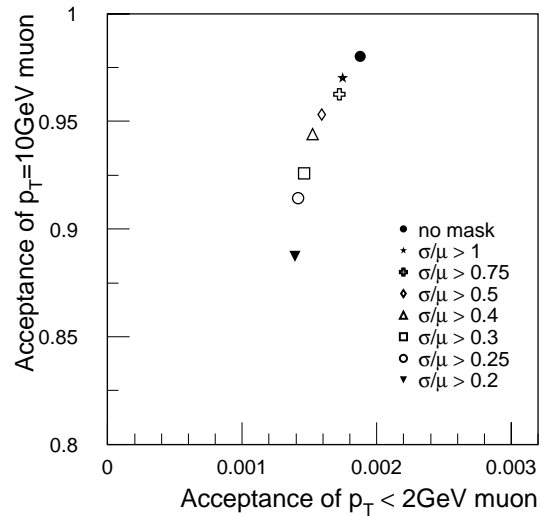
**Figure 14-22** Trigger efficiency for the end-cap system as a function of  $p_T$  for the 20 GeV  $p_T$  threshold, for various  $\eta$  ranges.



YH13V06

**Figure 14-23** Source of efficiency from muons below threshold for the low- $p_T$  end-cap system. Hit positions of muons below threshold triggered by the low- $p_T$  system with  $p_T^{\text{th}} = 6 \text{ GeV}$  are shown. The generated  $p_T$  was: a)  $< 2 \text{ GeV}$ ; b)  $2\text{--}3 \text{ GeV}$ ; c)  $3\text{--}4 \text{ GeV}$ ; d)  $4\text{--}5 \text{ GeV}$ .

One approach to reducing the rate from such low- $p_T$  muons is to ‘mask’, or remove from input to the coincidence logic regions known to have poor momentum resolution. However it should be noted that a significant fraction of these triggers lie outside the poor resolution regions. Figure 14-24 shows the trigger efficiency for 2 GeV muons in the low- $p_T$  system plotted versus the trigger acceptance for 10 GeV muons, when  $\eta$ - $\phi$  regions with poor momentum resolution are masked. It can be seen that the rejection of low- $p_T$  muons is weakly increased when the masking procedure is used, at the price of a visible efficiency loss for higher- $p_T$  muons.

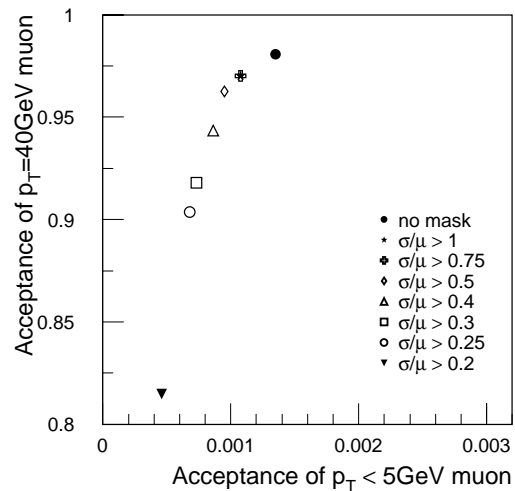


YH15V03

**Figure 14-24** The effect of masking on the low- $p_T$  trigger in the end-cap system. Trigger efficiency for muons with  $p_T < 2$  GeV is shown versus that for 10 GeV  $p_T$  muons, for various masking schemes. The trigger threshold is 6 GeV.

The situation is similar for the high- $p_T$  trigger threshold. The lower- $p_T$  muons triggered with high threshold are more focused in the regions with poor momentum resolution than in the low- $p_T$  case, as shown in Figure 14-25. However, randomly distributed triggered muons in the pivot plane are seen, particularly in the forward regions. An analysis of these triggers indicates that these are made by an accidental coincidence of the muon track and accompanying soft electrons.

Figure 14-26 shows the 5 GeV muon-trigger efficiency plotted against the trigger acceptance for high- $p_T$  muons in the high- $p_T$  end-cap system with 20 GeV threshold, when  $\eta$ - $\phi$  regions with poor momentum resolution are masked in the high- $p_T$  system. In this case the masking of bad regions is moderately successful in reducing further the trigger rate from lower- $p_T$  muons poorly measured by the system.



YH16V03

**Figure 14-26** The effect of masking on the high- $p_T$  trigger in the end-cap system. Trigger efficiency for muons with  $p_T < 5$  GeV is shown versus the trigger efficiency for 40 GeV  $p_T$  muons for various masking schemes. The trigger threshold is 20 GeV.

#### 14.5.4 Threshold flexibility

An important requirement of the muon-trigger system is that it possesses the flexibility to vary in small steps the trigger threshold across the range of  $p_T$  from 6 to 30 GeV; this allows the trigger rate to be reduced according to the background conditions and to produce RoIs for the Level-2 trigger with the lowest threshold possible.

Whilst the 6 and 20 GeV thresholds are those for which the trigger system has been optimized it is important to demonstrate the flexibility of the trigger to set thresholds other than these. This performance is illustrated here by the threshold flexibility of the end-cap system.

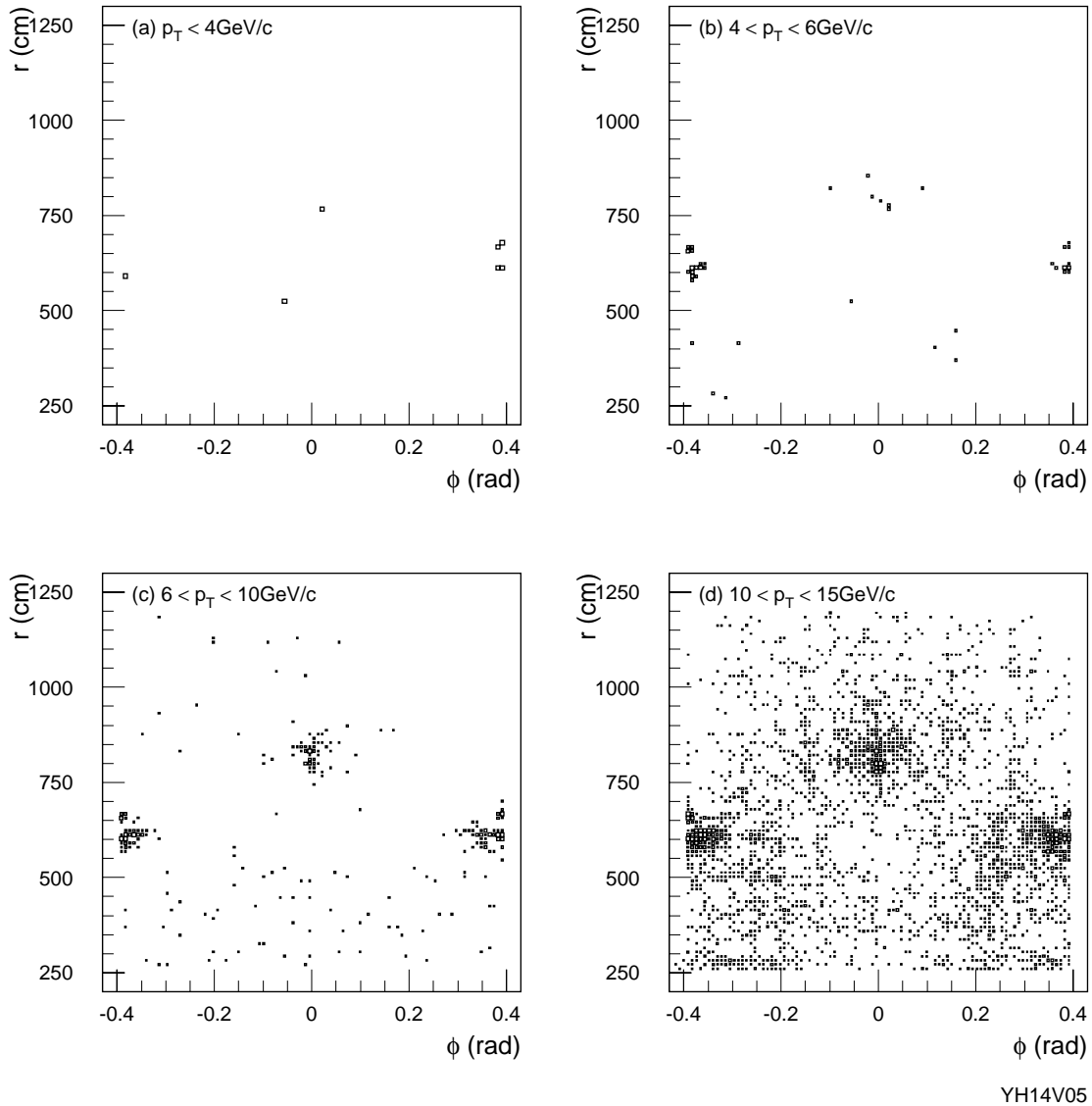


**Figure 14-25** Source of efficiency below threshold for the high- $p_T$  end-cap system. Hit position of muons triggered by the high- $p_T$  system with  $p_T^{\text{th}} = 20$  GeV is shown. The generated  $p_T$  was: a)  $< 4$  GeV; b)  $4\text{--}6$  GeV; c)  $6\text{--}10$  GeV; d)  $10\text{--}15$  GeV.

There are two points to be investigated:

- the consequence, for the full system, of setting a threshold as high as 30 GeV;
- the ‘cross-over’ transverse-momentum threshold from the low- $p_T$  system to the high- $p_T$  system.

The physical quantities to be analysed are the coincidence window size and the discrimination power to reject muons with  $p_T$  below threshold.

Figures 14-27 and 14-28 show the range of coincidence-window sizes for the end-cap low and high- $p_T$  systems, respectively, as a function of  $p_T$  threshold. The trigger-efficiency curves for each of these thresholds are shown in Figure 14-29.

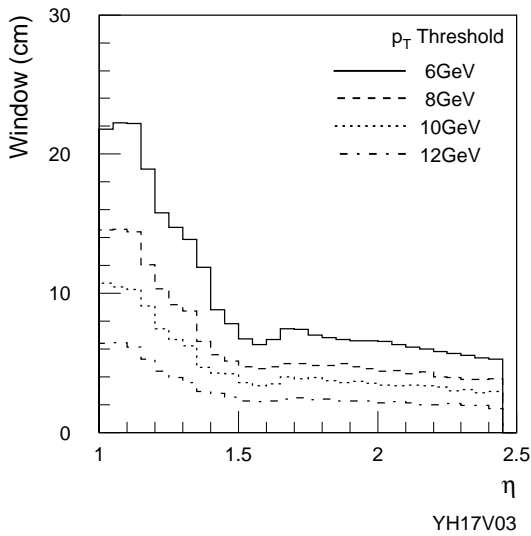


**Figure 14-27** Coincidence window size in the main bending direction averaged over  $\phi$ , as a function of  $p_T$  threshold, for the end-cap low- $p_T$  system.

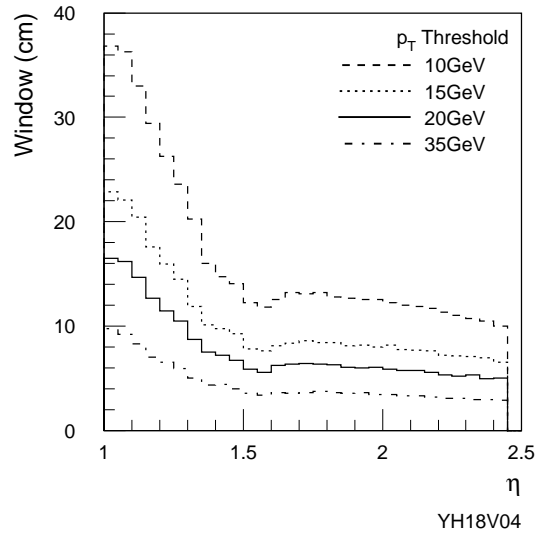


**Figure 14-28** Coincidence window size in the main bending direction averaged over  $\phi$ , as a function of  $p_T$  threshold, for the end-cap high- $p_T$  system.

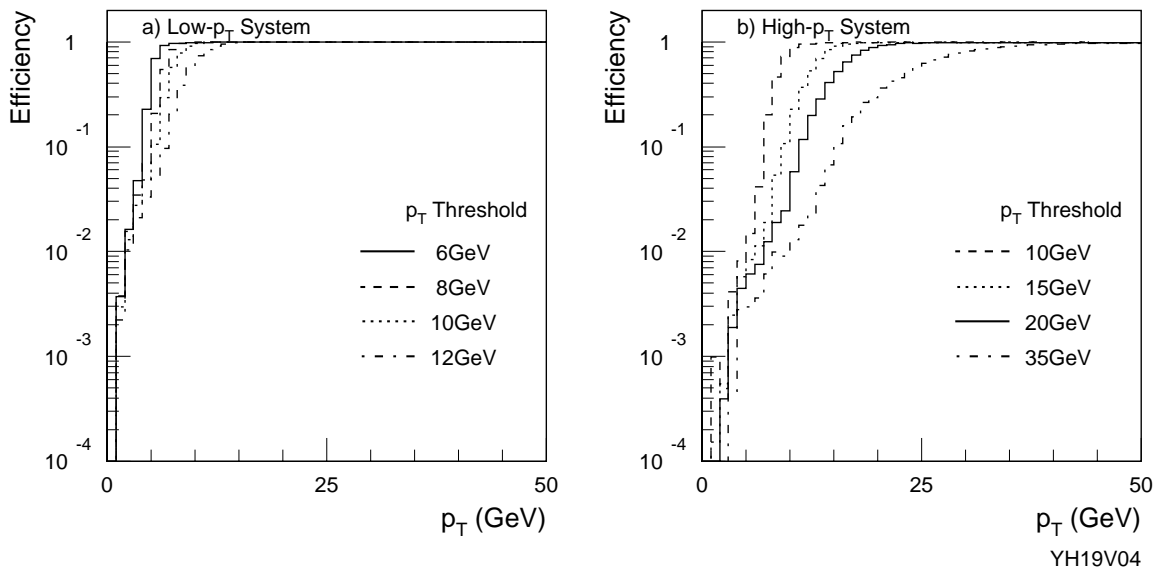


**Figure 14-29** Trigger efficiency curves for a range of  $p_T$  thresholds for (a) low- $p_T$  and (b) high- $p_T$  end-cap trigger systems.

The consequences of this study are the following.

- The low- $p_T$  system can be used to set a threshold as high as 10 GeV in the end-cap system. The main limitation arises from the trigger-detector granularity.
- The high- $p_T$  system can be used to set a threshold at 10 GeV with efficiency close to 1. Thus we have a significant overlap in the threshold potential between the high and low- $p_T$  systems in the end-cap. Being able to use the high- $p_T$  logic at such low thresholds allows the possibility of an extremely robust trigger for b physics in the event that background conditions prevent the low- $p_T$  logic from being usable.

- Thresholds significantly above 10 GeV/c can be set only using all planes of the trigger system, i.e. by using the high- $p_T$  plane additionally. The consequence of this is a coincidence window size almost twice as large as that at 20 GeV.

The detector and trigger simulation has been used to optimize the granularity of the end-cap trigger counters and to determine the dimension of coincidence matrices. This has been done using the single muon data generated for the above studies and producing a read out segmentation scheme (in terms of a wire grouping in the  $r/\eta$  direction) that optimizes the performance requirements of the trigger (as set out in [14-1]) with the constraint on the total number of channels arising from cost limits. The final segmentation contains 220,000 wire channels and 95,000 strip channels. The inputs to the coincidence matrices from the wire groups consist of 31  $\delta r$  inputs (in the range  $-15$  to  $+15$ ) and 15 from  $\delta\phi$  inputs ( $-7$  to  $+7$ ). Details of the coincidence matrices and their inputs can be found in Chapter 12.

## 14.6 Trigger rates: prompt and secondary muons

The rates that will be seen in the ATLAS level-1 muon-trigger have been calculated by performing a full Monte Carlo simulation of the response of the ATLAS detector and level-1 muon-trigger to single muons to extract trigger efficiencies as a function of muon  $p_T$  and  $\eta$ . These efficiencies have then been convoluted with cross-sections extracted from Monte Carlo simulation of the physics processes that give rise to muons in the detector. This procedure has been performed for prompt single-muon production, from b and c hadrons and from W and Z decays, and for decays in flight to muons of  $\pi$  and K mesons.

The response of the detector and trigger ensemble to muons produced by the interaction of the beam and the LHC machine components ('beam halo'), as well as to cosmic muons, has been investigated through dedicated Monte Carlo studies.

### 14.6.1 Acceptance to muons from interaction products

#### 14.6.1.1 Cross-sections of prompt processes and meson decays in flight

Inclusive muon cross-sections at LHC arising from decays of b and c hadrons, of top quarks and of W and Z decays have been calculated using the Monte Carlo program Pythia, version 5.7 [14-11]. These cross-sections, integrated in the kinematic region  $|\eta| < 2.7$  and  $p_T > 3$  GeV, are shown as a function of  $p_T$  in Figure 14-30. The cross-sections are dominated by semileptonic decays of b and c hadrons for  $p_T > 8$  GeV.

Light hadrons emerging from p-p collisions contribute charged-particle background via two mechanisms:

- decays in flight (hadron  $\rightarrow \mu X$ ) in the inner tracker cavity,
- hadronic debris produced in calorimeter showers and in other interaction between hadrons and detector components.

Here we consider the consequence on the trigger rate of the secondary muons originating from the  $\pi/K$  decays. The cross-sections of such muons have been calculated using the DPMJET Monte Carlo program [14-12], and the results are shown in Figure 14-30. In the calculation the

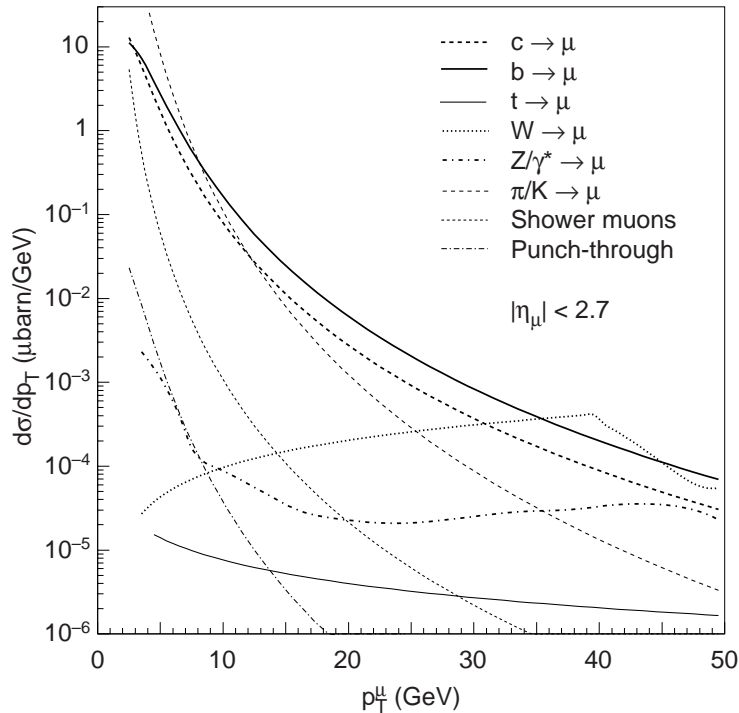


**Figure 14-30** Muon cross-sections as a function of  $p_T$  at production, integrated in the region  $|\eta| < 2.7$ .

total inelastic pp cross-section is normalized to 80mb. The Pythia 5.7 program has been used as a check of this cross-section. At lower transverse momenta ( $p_T < 8$  GeV) in-flight decays of  $\pi$  and K mesons are the dominant source of muons and thus of trigger rate in the level-1 muon system.

#### 14.6.1.2 Rates from prompt muons and meson decays in flight

The calculated trigger efficiencies for single muons have been convolved with the cross-sections plotted in Figure 14-30 to yield the total expected trigger rate from each production process in the barrel, end-cap and the sum of the two systems. In the end-cap this convolution has been performed in three bins of  $\eta$  to account for the significant dependence on  $\eta$  of both the cross-section and the efficiency of the level-1 trigger in the end-cap. In the barrel such a treatment is not necessary. The estimated rates are shown in Table 14-4.

The source of this rate varies in each of the two subsystems and for the process involved, although in almost all regions of the detector the rate arises largely from muons from in-flight decays of  $\pi$  and K mesons. This rate derives almost exclusively from lower- $p_T$  (less than a few GeV) muons seen in the trigger detectors in the region  $1.5 < |\eta| < 2$ . Such muons are not seen in the barrel due to the shielding effect of the calorimeter material.

#### Uncertainties in trigger rates

Uncertainties in the trigger rate arise from several sources:

- The prompt rate is a small fraction of the total rate seen by the level-1 muon-trigger at low- $p_T$  and less than half at high- $p_T$ , and so its uncertainty does not dominate the errors on the total-rate estimate. There are however significant uncertainties in the prompt muon cross-sections estimated by Pythia at LHC energies. The most important of these

**Table 14-4** Trigger rates, in kHz, expected in the barrel, end-cap and combined muon system arising from various physics processes. These rates are calculated by convolving the single muon cross-section from each process with the efficiency of the level-1 trigger to single muons. The low- $p_T$  rates assume a luminosity of  $1 \times 10^{33} \text{ cm}^{-2}\text{s}^{-1}$  and the high- $p_T$  rates a luminosity of  $1 \times 10^{34} \text{ cm}^{-2}\text{s}^{-1}$ .

	Process	Barrel	End-cap	Combined system
<b>Low-<math>p_T</math> (6 GeV)</b>	$\pi$ / K decays	7.0	9.8	16.8
	b	1.9	2.1	4.0
	c	1.1	1.3	2.4
	W	0.004	0.005	0.009
	<b>Total</b>	<b>10.0</b>	<b>13.2</b>	<b>23.2</b>
<b>High-<math>p_T</math> (20 GeV)</b>	$\pi$ / K decays	0.3	1.8	2.1
	b	0.4	0.7	1.1
	c	0.2	0.3	0.5
	W	0.035	0.041	0.076
	<b>Total</b>	<b>0.9</b>	<b>2.8</b>	<b>3.8</b>

originate from the unknown factorization and renormalization scales in the structure functions and the running coupling constant; these are likely to introduce cross-section uncertainties at the level of a factor two. Additional uncertainties arise from the unknown quark mass, yielding a factor of 1.5 on the total uncertainty. The accuracy with which cross-sections measured at the Tevatron are reproduced by the simulation used here gives an indication of the total size of such uncertainties. The model used here is consistent with inclusive b-production rates measured by the CDF experiment [14-13]. The extrapolation of cross-sections at Tevatron energies to those at the LHC introduces uncertainties less than a factor of two [14-14]. However all of these quantifications of uncertainties in the cross-section apply to the region  $p_T > 6\text{GeV}$ . The uncertainties in cross-sections at  $p_T$  values far below this (such as  $p_T \sim 2\text{GeV}$ , where the majority of the level-1 muon-trigger rate originates) are likely to be greater and no authoritative estimates are available.

- Uncertainties in the modelled muon rate from in-flight decays of light mesons are dominated by model dependence and the parameters governing the parton showering and hadronization. An indication of the uncertainties in the cross-section estimation has been obtained by comparing two independent Monte Carlo programs. All rate calculations have been performed using DPMJET, giving the rates discussed above, and with Pythia as a cross-check. The two programs have been optimized independently and so can be expected to reflect the divergence of the different approaches to modelling of the cross-section. Whilst Pythia has the possibility to describe soft processes, DPMJET is a dedicated simulation of inelastic hadron collisions tuned to existing data. (Both programs here are normalized to a total inelastic cross-section of 80mb.) Whilst the differential cross-sections  $d\sigma/dp_T$  and  $d\sigma/d\eta$  modelled by the two programs are of rather similar shape, Pythia consistently produces a somewhat lower cross-section than DPMJET. For this reason the rate estimate obtained using the Pythia cross-section is typically 35% lower than that from DPMJET. This discrepancy is considered to be an indication of the systematic uncertainties on this cross-section, particularly with regard to the modelling of

the  $p_T$  distribution. Uncertainties on the total inelastic cross-section are likely to be smaller than 30%.

- The limited statistics of the efficiency calculation result in significant uncertainties on the total accepted rate. This is particularly true of the  $\pi/K$  decays where the accepted rate is a result of the convolution of a very low efficiency with a very high cross-section. The statistical uncertainties on the accepted rate are of the order 10–15%, and are thus generally small in comparison with the expected model uncertainties on the input physics processes.
- In principle the rate can depend upon the accuracy of the modelling of the detector response and the ongoing optimization of the detectors themselves. (In the end-cap for example the rate studies were performed using a read out segmentation that is slightly different from that which the current optimization yields.) In general however the effect the detector response will have on the final rate is small not least because of the declustering algorithms which ensure that at various stages in the trigger chain the multiplicity of hits is highly controlled. Whilst the details of the detector response and the interaction with the declustering algorithms do introduce uncertainties on the above rates they are expected to be small. During studies of the efficiency of the level-1 trigger the effect of substantial changes in the amount of passive material in the ATLAS detector has been investigated; these changes have been found to significantly affect rates, since these are dominated by rather soft muons. The material modelled by the ATLAS detector simulation is a rather accurate representation of the currently envisaged design and future developments are likely to involve the addition of material (such as cables, cooling structures, etc) rather than its removal, and these in turn are likely to suppress rather than enhance the total trigger rate from prompt and secondary muons.

Similarly the optimization of the read out segmentation of the trigger detectors, particularly in the case of the wire grouping of the TGC chambers in the end-cap, will affect the sharpness of the threshold that can be set in the trigger. However the optimal segmentation, given the cost constraints on the number of channels in the total system, is rather close to that in the trigger simulation used here, and it is expected that this uncertainty will change total rates rather marginally.

Masking of low-resolution regions in the detector, again most relevant in the end-cap (see Figure 14-10), is foreseen. This will serve to reduce rates at the expense of acceptance. Such possibilities are currently under study, and it is expected that the rate in the end-cap can be reduced by a few tens of per cent. The analysis of real ATLAS data will allow an optimal masking scheme to be implemented.

## 14.6.2 Trigger rate from non-proton-proton muons

### 14.6.2.1 Cosmic muons (barrel system)

Despite the significant depth at which the ATLAS experiment is situated, cosmic rays contribute to the trigger rate in the muon system. This rate arises largely from the access shafts located above the experimental hall. The ATLAS cavern is located about 75 m underground and access made possible by two parallel shafts (9 m and 12.6 m in diameter) about 60 m deep. The axes of both shafts are centred on the beam line and they are separated by a distance of 25 m.

Cosmic muons [14-15] have been simulated at ground level above the experimental area and propagated through the shafts and the rock using Monte Carlo techniques. Muons reaching the experimental hall have then been tracked through the ATLAS detector and trigger simulation. The first 14 m of material below ground level have a density of  $1.6 \text{ g/cm}^3$ ; the remaining material down to the experimental hall has been simulated as rock with  $2.5 \text{ g/cm}^3$  density. To reach the ATLAS detector, a perpendicular muon traversing the full depth of rock must have an energy above 20 GeV.

The surface used for the generation of cosmic muons was a square at ground level centred on the detector position with a side of length that has been varied from 80 m to 150 m. Hits recorded by the RPC system have been passed through the trigger simulation; the ratio of the number of triggered muons to the number generated at the surface gives the trigger probability per incident muon for the given area of cosmic production. The trigger rate from cosmic muons is given by the rate of muons incident on the generation area multiplied by the calculated trigger probability. The trigger rate has been studied as a function of the area dimension in order to evaluate the edge effects due to the limited size of the production surface.

By normalizing the incident cosmic rate to  $100 \text{ Hz/m}^2$  (the approximate rate of the muon component at sea level), we found a trigger rate in the low- $p_T$  system (for a 6 GeV  $p_T$  threshold) below 200 Hz. The corresponding rate for the high- $p_T$  system (for a 20 GeV threshold) is much lower (below 10 Hz). This rate is more than one order of magnitude lower than the rate from pp interaction muons, but still sufficient to offer the potential for their use in the calibration of the muon-trigger in the barrel region.

Figure 14-31 shows the  $\eta$ - $\phi$  scatter of cosmic muons that give a trigger in the barrel low- $p_T$  system. Most of the triggered muons are in the central region of the detector, in the top and the bottom of the muon-trigger system, as might be expected. It is expected that cosmic muons, given the estimated rate calculated here, can be used to calibrate the muon-trigger in the barrel region, potentially for both geometrical alignment and timing studies. This valuable data can be exploited far in advance of the first beams in LHC.

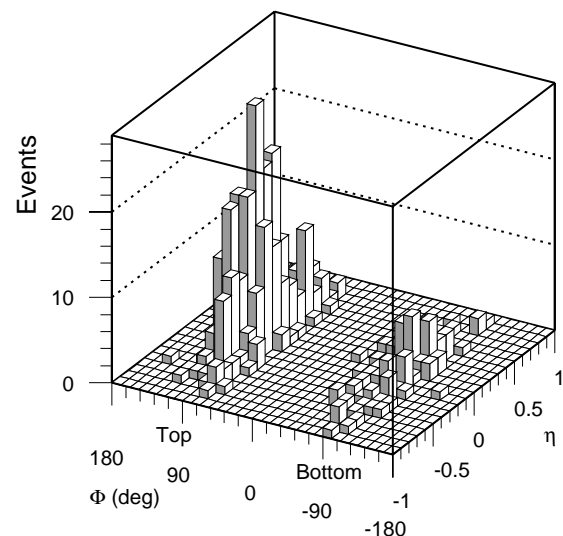


**Figure 14-31** Cosmic muons in the barrel system.  $\eta$ - $\phi$  coordinates of cosmic muons triggering the low- $p_T$  trigger system ( $p_T$  threshold of 6 GeV).

#### 14.6.2.2 Beam halo muons (end-cap system)

It has long been known at hadron colliders that very substantial muon fluxes can be seen, particularly in the more forward regions, arising from muons produced through the interaction of the proton beam with residual beam gas in the beam pipe, and with the limiting apertures of the machine such as collimators. The muons are produced largely at a small angle relative to the beam direction and at low radius, and can have potentially catastrophic implications for the rate of muon-triggers seen in these regions. In this respect the experience of previous detectors has been valuable, and the projective geometry of the end-cap muon-trigger chambers serves to control this problem.

A comprehensive study of muons produced in interactions between the LHC beam and the machine components has been performed for the CMS experiment using a detailed simulation of such processes [14-16], considering the latest information on the design of the LHC machine. The differences between the beam conditions in ATLAS and CMS are slight enough that this simulation is also entirely relevant for ATLAS. The interactions modelled are those of a beam of 530 mA at 7 TeV with luminosity  $1 \times 10^{34} \text{ cm}^{-2}\text{s}^{-1}$ , with all machine components within 1000m of the interaction point simulated. The muons produced in such interactions have an energy distribution very sharply peaked at energies of a few GeV and with a tail extending to 500 GeV. The greatest flux of muons at the cavern entrance is below a radius of  $\sim 1\text{m}$  relative to the beam line, well below the geometrical acceptance of the end-cap muon-trigger chamber, but extending to the limit of the wheel of TGC chambers in the pivot plane. The mean angle of these muons to the beam-line is 60 mrad. The flux of muons from the simulation at the entrance to the ATLAS cavern ( $|z| \sim 26.5 \text{ m}$ ) and in the pivot plane of the end-cap trigger counters ( $|z| \sim 14\text{m}$ ) is shown in Figure 14-32. The counting rate per detector plane in each end-cap from such muons is  $\sim 60 \text{ kHz}$ .

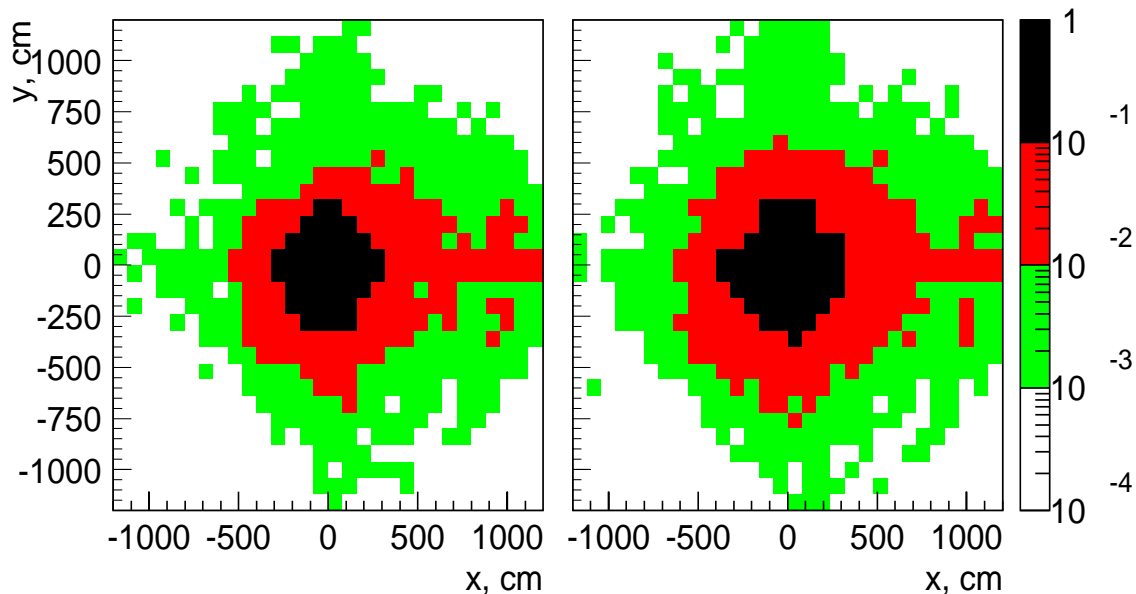


**Figure 14-32** The flux of muons at (a)  $|z| \sim 26.5 \text{ m}$ , the entrance to the experimental hall, and (b)  $|z| \sim 14\text{m}$ , the position of the pivot plane of the TGC counters, as modelled by [14-15]. Units are muons  $\text{cm}^{-2}\text{s}^{-1}$ .

These simulated muons from beam-loss processes have been passed through the full ATLAS detector and trigger simulation to estimate the rate in the end-cap level-1 muon-trigger.

The estimated rates arising from the halo muon flux are 250 Hz and 16 Hz for the 6 GeV and 20 GeV low- and high- $p_T$  triggers respectively. These rates are negligible in comparison with the rates from interaction products, and can contribute significantly to the trigger rate only if the halo rate here is underestimated by a factor of ten or more; in this instance the rate would still be quite tolerable.

## 14.6.3 Dimuon-trigger rate

### 14.6.3.1 Two-muon physics reactions

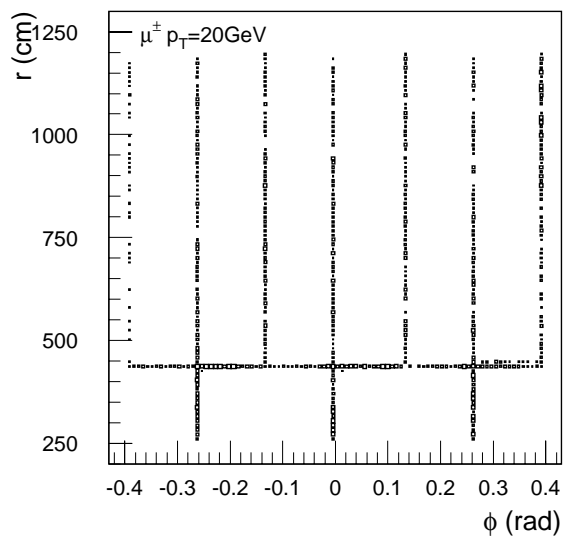
The rate of dimuons from the process  $bb \rightarrow \mu\mu X$  has been extracted using the Pythia Monte Carlo. This process dominates all other sources of dimuon production where both muons have  $p_T < 20$  GeV. For  $p_T \sim 20$  GeV Z decays have a similar dimuon production cross-section and above this point Z products dominate. For the purposes of providing a b-physics trigger, demanding two muons that both pass the nominal low- $p_T$  threshold (6 GeV) yields genuine dimuon events almost entirely from b-decays. The integrated cross-section for the process  $bb \rightarrow \mu\mu$  in the region  $|\eta| < 3$ , where both muons have  $p_T > 6$  GeV, is  $0.03 \mu\text{b}$ , in reasonable agreement with previous calculations made using ISAJET [14-17]. The total rate from genuine high- $p_T$  dimuon b-events is thus very small compared with the single-muon rate for the same  $p_T$ .

### 14.6.3.2 Trigger rate from double-counted single muons

#### In the end-cap

When a muon traverses the overlapping edges of neighbouring trigger sectors, it can produce a trigger in each of the trigger sectors. In the end-cap trigger system, efforts to both minimize such double triggers and avoid inefficiency in the overlap regions have been made as described in Section 14.4. Despite this, small overlap regions remain. Figure 14-33 shows, as an example, the position in station 3 of 6 GeV single muons which are doubly triggered by the end-cap low- $p_T$  trigger system.

The vertical bands in the figure are due to the overlap of neighbouring trigger sectors by half a strip width. The horizontal band located around a radius of 437 cm is also due to the overlap of the trigger sectors in which the patch-panel logic can not be applied owing to the different chamber layout between the end-cap and forward regions. The current design has at most 3.5 cm of overlap between neighbouring sectors, which has yet to be optimized by using specially modified strips in this region; such an optimization will reduce double triggers.



YH20V04

**Figure 14-33** Hit positions of doubly triggered muons in the end-cap pivot station for 20 GeV  $p_T$  muons. The double triggers are due to overlaps between neighbouring trigger sectors.

The fraction of the double-triggered muons to muons generated in an  $|\eta|$  region of 1.2–2.35 is summarized in Table 14-5. These fractions imply a rate at nominal LHC luminosity  $\sim 4$  kHz. Efforts are being made to find strategies to reduce the double-counting rate further.

**Table 14-5** The fraction of doubly triggered muons in the low- $p_T$  system, as a fraction of muons generated in the region  $1.2 < |\eta| < 2.35$  in the end-cap muon-trigger.

	6GeV	20GeV
$\mu^+$	$1.6 \pm 0.1\%$	$2.2 \pm 0.1\%$
$\mu^-$	$1.9 \pm 0.1\%$	$2.4 \pm 0.1\%$

The fraction of the geometrical overlap to the total area of the end-cap trigger counters is estimated to be about 2.5%. The difference between the estimate and the results of the simulation is due to the incident angle of muons to the counters. The double triggers in the transition region between the barrel and end-cap are not shown in Figure 14-33, but are solved by logic in the muon central trigger processor interface, MUCTPI (see Chapter 13).

### In the barrel

In the barrel the major source of double-counted single muons is the overlap in the  $r$ - $\phi$  projection of the large and small sectors. This overlap is necessary to provide a level-1 muon-trigger for tracks crossing both large and small chambers, which are used for the calibration of the alignment system of the muon spectrometer. During normal operation of the experiment an appropriate masking of the  $\phi$  strips located in the overlap regions will be applied. The optimization study of the single-muon-trigger acceptance against the rejection of double-counted single muons is in progress.

## 14.7 Fake trigger rate

A large background flux is expected at LHC due to the interaction of hadrons arising from the proton-proton interactions with the forward elements of the ATLAS detector, the shielding system and machine elements such as the beam pipe and collimators to produce neutrons in the experimental hall. Thermal neutrons thus produced are absorbed by nuclei and emit photons of an energy 10–1000 keV. Hadrons and muons are also produced in cascade processes. The particles thus produced can induce high counting rates in the muon-trigger chambers. Here we estimate the rate induced in the ATLAS level-1 trigger from such backgrounds.

The background flux and rate seen in the level-1 trigger have been evaluated using the FLUKA Monte Carlo program [14-18]. This Monte Carlo program is not that used for the standard simulation of high-energy physics processes; it can track particles at very low kinetic energies. In particular, neutrons are propagated down to thermal energies. The shielding layout of the ATLAS detector used here is version ‘TP32’, as discussed in [14-19]. The shielding layout envisaged by the TP32 scheme has changed significantly in the current design; however the study and optimization of the new shielding scheme compatible with the most recent changes to the muon system layout has shown neutron and photon fluxes very close to those seen with TP32. The statistics accumulated with charged particles is, however, still insufficient. For this reason we have used the higher statistics results available from TP32 for the study of the accidental trigger rate.

Background can be classified into three classes:

- Background particles that produce a hit in a single trigger counter.

Background originating from soft Compton electrons ( $E < 2$  MeV) and neutron-induced soft protons is produced in the chamber wall or the gas of the detector and absorbed by

the material of the same detection unit. This does not introduce correlations between hits detected in different muon-trigger counters. The counting rate from this background at nominal LHC luminosity is  $5.2 \text{ Hz/cm}^2$  in the barrel and  $4.5 \text{ Hz/cm}^2$  in the end-cap. Figure 14-34 shows typical fluxes in the second station of the precision muon system.

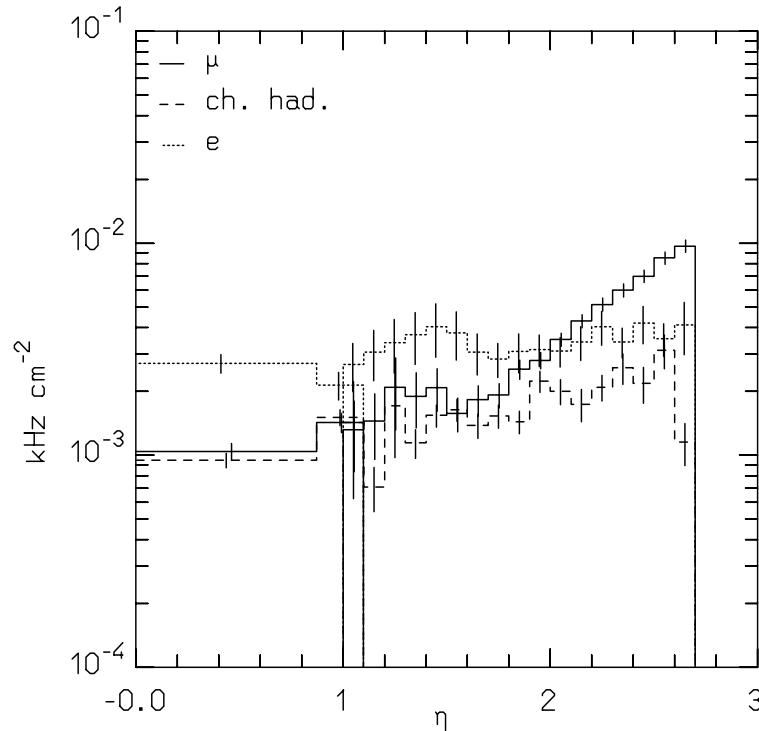


**Figure 14-34** Charged-particle background fluxes, for muons, charged hadrons and electrons, as a function of rapidity at the second station of the MDT chambers, close to the muon-trigger counters. This data is from the FLUKA simulation.

- Background particles that can produce hits in two adjacent trigger counters.

Hard Compton electrons with energy above 2 MeV and soft protons: These particles are absorbed in  $\sim 3 \text{ g/cm}^2$  of the typical material of the trigger counters. This background produces correlated hit patterns in trigger counters belonging to the same trigger station. Counting rates from this background at nominal LHC luminosity are  $2.0 \text{ Hz/cm}^2$  in the barrel and  $3.1 \text{ Hz/cm}^2$  in the end-cap.

- Background particles that can produce correlated hits in more than one muon-trigger station.

Hard protons, pions and muons having momentum  $\sim 100 \text{ MeV}$ , sufficient to cross not only neighbouring trigger planes within a station, but traverse closely spaced planes of a trigger station, such as the two planes of the low- $p_T$  system. Such a particle can produce a correlated hit pattern simulating a true muon-trigger. Detector simulation by FLUKA predicts a substantial rate for these relatively energetic particles:  $\sim 1.9 \text{ Hz/cm}^2$  and  $3.0 \text{ Hz/cm}^2$  in the barrel and end-cap, respectively, where approximately 60% of the rate comes from muons.

The following section will present a study of the first two types of background, i.e. those that produce hits in at most one trigger station. Section 14.7.2 will discuss fake trigger rate produced by penetrating particles.

### 14.7.1 Trigger rate from background hits in a single trigger station

A simplified version of the trigger-counter geometry and the trigger logic has been used to investigate the rate arising from soft ( $E < 2\text{MeV}$ ) background particles. Each of the trigger subsystems (barrel and end-cap) was divided into projective towers. The tower dimension is given by the counter size in the pivot plane. The size of a tower in the second and third trigger planes was determined by projecting from the nominal interaction point to the pivot plane counter. The calculation of the rate proceeds as described in [14-20].

In the rate calculation the coincidence of correlated hits from a single track with other background hits has been considered, accounting for the appropriate majority logic. It is seen that the rate due to this is much larger than that due to accidental coincidence of uncorrelated hits. However, only correlations in one trigger station are included and not the rate due to tracks that leave correlated hits in more than a single trigger station (see Section 14.7.2).

The rate calculation in the barrel system has been performed considering six counter planes (three doublets). It assumes two different scenarios for the majority logic in the outermost doublet: both one-out-of-two and two-out-of-two. Whilst the two-out-of-two coincidence provides a more robust logic and thus better rate performance, the one-out-of-two logic has been considered for the study because of its greater efficiency.

In the end-cap system seven planes of trigger counters are considered with the innermost station consisting of a triplet unit. This innermost station is used in the high- $p_T$  trigger where the majority logic used is two-out-of-three in the  $r$ -plane, and one-out-of-two in  $\phi$ . The low- $p_T$  trigger logic is the same as in the barrel and the calculation proceeds in the same way.

In the calculation of the rate expected in the high- $p_T$  systems (for both barrel and end-cap) the coincidences of prompt muons with background hits are also taken into account. This effect introduces a linear dependence of the fake trigger rate on the background flux and a quadratic dependence on the luminosity.

Figure 14-35 compares the fake trigger rate (for both the nominal background flux and the flux multiplied by a factor of five and ten, for the low luminosity, and ten, for the high luminosity) with the rate expected from prompt muons and in-flight decays of  $\pi$  and K mesons as a function of luminosity. The result is presented for the low- and high- $p_T$ -triggers (at nominal thresholds) for the barrel and the end-cap.

The dominant contribution to the fake low- $p_T$  trigger rate in both barrel and end-cap is due to the coincidence of a pair of hits from a penetrating particle in one of the low- $p_T$  stations, with one or more hits deposited by any other particle. The fake high- $p_T$  trigger rate is dominated by a low- $p_T$  trigger in coincidence with any other hit (or track) in the high- $p_T$  station of the barrel or end-cap.

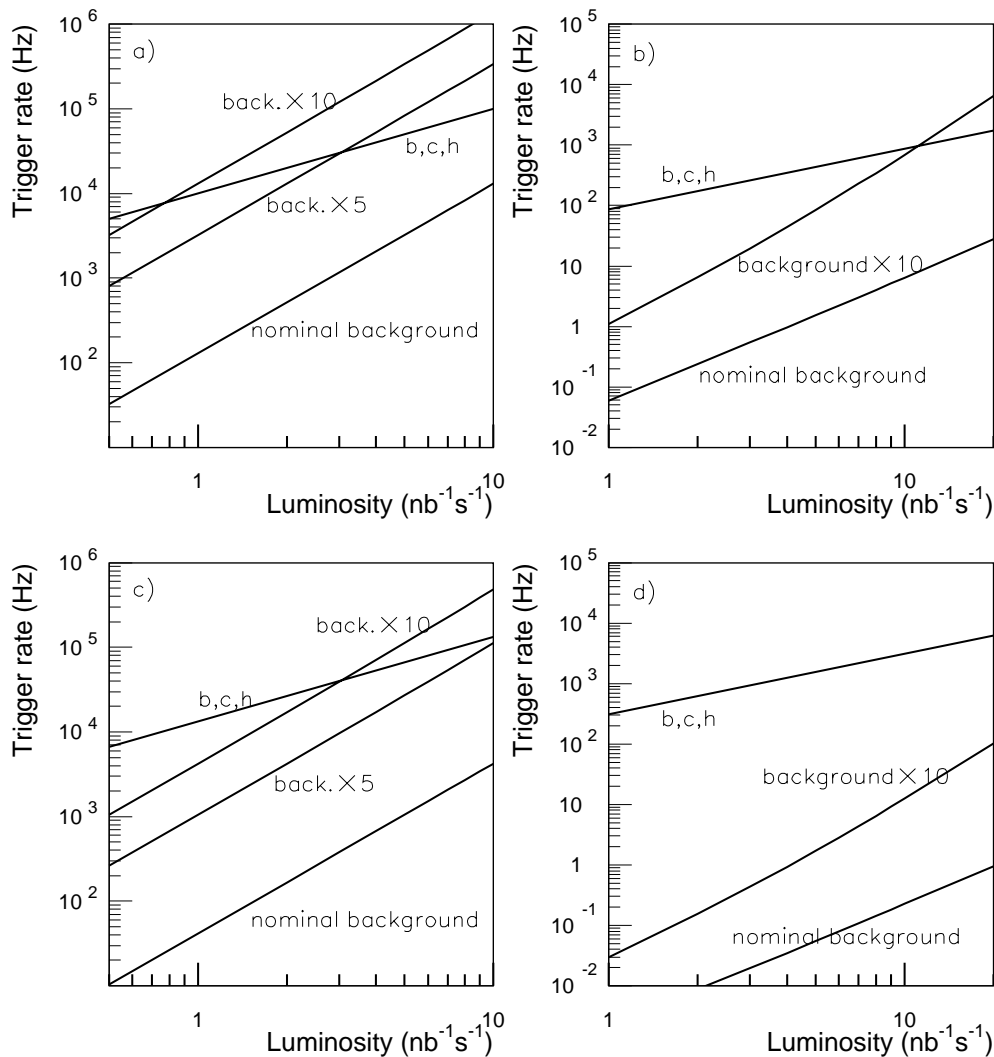


**Figure 14-35** The accidental trigger rate from soft background particles compared with the rate expected from prompt muons (b, c, h) as a function of luminosity, for a) barrel trigger, low- $p_T$  6 GeV threshold; b) barrel trigger, high- $p_T$  20 GeV threshold; c) end-cap trigger, low- $p_T$  6 GeV threshold; d) end-cap trigger, high- $p_T$  20 GeV threshold.

## 14.7.2 Trigger rate from hard background particles

Monte Carlo studies of hard ( $E > 10$  MeV) charged particles in the ATLAS cavern predict that whilst the rate of electrons with energy large enough to cross two muon stations is very small, there is a substantial flux of muons, charged pions, protons and charged kaons. The expected flux at nominal LHC luminosity of muons and pions is 1.1 Hz/cm<sup>2</sup> and 0.5 Hz/cm<sup>2</sup>, respectively, in the barrel and 2.1 Hz/cm<sup>2</sup> and 0.6 Hz/cm<sup>2</sup> in the end-cap. This flux leads to a significant background rate in the level-1 muon-trigger system. The momentum of these particles is in the range 50 to 200 MeV, Figure 14-36. Such background particles can penetrate trigger-detector components and produce a trigger coincidence consistent with that from a

prompt muon, in particular in the low- $p_T$  system, where only a two-plane coincidence is required.

The processes in the Monte Carlo program that yield this particle flux as well as their angular distribution are not yet known and a dedicated analysis is ongoing. In the absence of detailed information about these particles a few possible scenarios as to their origin and angular distribution were assumed in a simulation study that has been performed to assess possible trigger rates due to this flux.

Preliminary results of this simulation study indicate that the level-1 trigger rate from this background is potentially problematic. This study is preliminary and it will be repeated when more information is available about the origin and nature of this background. In parallel to this study, the muon-trigger group is contemplating scenarios to make the trigger more robust against such backgrounds.

Several solutions are being considered:

- For the single low- $p_T$  muon-trigger (at low luminosity), add a loose coincidence with the plane used in the high- $p_T$  trigger to confirm the origin of the muon track from the vertex. This can be implemented in the “non-bending” projection for the barrel and in both projections for the end-cap with no change in the electronics design of the muon-trigger. The consequence (to be verified) is a possible increase of the lowest  $p_T$  threshold that can be set. Initial studies of this solution have given encouraging results.
- Demand an additional coincidence of the muon in the level-1 muon system with associated calorimeter cells. The tile calorimeter [14-21] has demonstrated good separation of the muon signal from the electronic and physics noise of the detector, and this could be used in conjunction with the level-1 muon system in the barrel. In particular, the third sampling appears very attractive for this purpose, although the modifications to the design of the front-end electronics that would be required to make available the additional signals have not yet been studied in detail. However, the tile calorimeter only extends to  $|\eta| \sim 1.5$ .
- Utilizing the end-cap calorimeter for muon confirmation in the level-1 trigger, although not impossible, appears quite difficult and would imply a considerable redesign of the end-cap calorimeter electronics.
- For the level-1 trigger in the end-cap muon system, another possibility is to demand the additional coincidence of the innermost TGC station, situated between the forward calorimeter and the end-cap toroid. This inner station is not nominally used in the trigger, being foreseen only to measure the second coordinate of muon tracks with  $|\eta| > 1$ . This solution implies a significant extension to the present design of the forward trigger electronics, and can be considered only after a detailed and complete study of the hard charged-particle background. The study must consider the trigger rate for the present

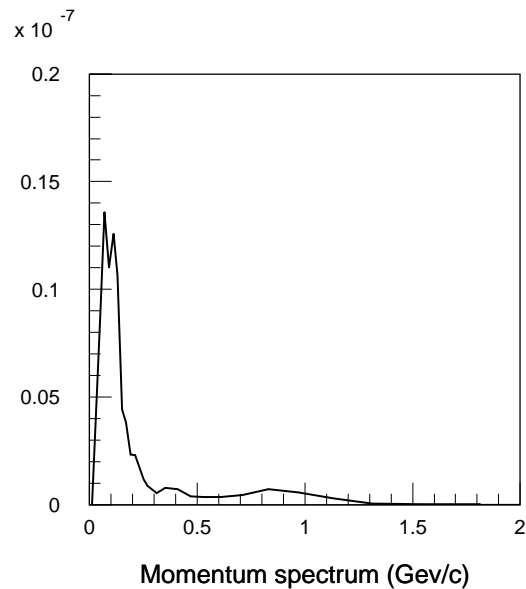


**Figure 14-36** The momentum spectrum of the background responsible for most of the rate induced.

forward trigger design and for that including the innermost TGC station, to evaluate the overall benefit of this approach.

However, by far the most important step to be performed by the ATLAS community is a very detailed analysis of the physics processes which lead to the production of such high-momentum background particles, in conjunction with the identification of the regions where these processes mostly occur. Further optimization of the shielding system of the ATLAS muon system must take place to identify solutions that reduce the hard charged-particle rate. Finally, experimental checks of the background rate in the LHC-like environmental conditions can help to quantify the reliability of the radiation-level estimates in the ATLAS hall.

## 14.8 References

- 14-1 *LVL1 Muon Trigger User Requirements Document (Draft version 1.4)*, ATLAS working document, ATL-DA-ES-0002, March 1998.
- 14-2 *ATLAS Trigger Performance Status Report*, CERN/LHCC/98-15, June 1998.
- 14-3 *GEANT 3 — Detector description and simulation tool*, CERN program library long write-up W5013, 1993.
- 14-4 *DICE manual*, ATLAS internal note SOFT-NO-10, 1994.
- 14-5 *ATRIG — ATLAS Trigger Simulation User Guide Revision 0.00*, ATALS note SOFT-94-017, 1994.
- 14-6 *ATLAS Muon Spectrometer Technical Design Report*, CERN/LHCC/97-22 ATLAS TDR 10, May 1997.
- 14-7 L. Chevalier et al., *AMDB\_SIMREC: A Structured data base for the ATLAS Spectrometer Simulation Program*, ATLAS note MUON-NO-148, 1997.
- 14-8 O. Jinnouchi and O. Sasaki, *Study of the muon level-1 trigger scheme for TGC*, ATLAS note DAQ-NO-82, 1998.
- 14-9 A. Nisati, *Preliminary timing studies of the barrel muon-trigger system*, ATLAS note DAQ-NO-83, 1998.
- 14-10 A. Rimoldi, *Geometrical acceptance for the trigger chamber system and study of the reaction  $H \rightarrow ZZ^* \rightarrow$  four muons from the acceptance point of view*, ATLAS note DAQ-98-119.
- 14-11 T. Sjöstrand, *PYTHIA 5.7 and JETSET 7.4 Physics and Manual*, CERN-TH.7112/93, 1993.
- 14-12 J. Ranft, *DPMJET version II.3 and II.4: sampling of hadron-hadron, hadron-nucleus and nucleus-nucleus interactions at cosmic ray energies, according to the Dual Parton Model description of the model and code manual*, INFN-AE-97-45.
- 14-13 P. Eerola, *The inclusive muon cross-section in ATLAS*, ATLAS note PHYS-NO-120, November 1997.
- 14-14 M. Mangano, *Heavy quark production*, LHC98 workshop, CERN, February 1998.
- 14-15 Particle Data Group, *Review of particle properties*, Phys. Rev. D54, 122, 1996 and references therein.
- 14-16 Drozhdin, et al., *Accelerator related background in the CMS detector at LHC*, Nucl. Instrum. Methods, A381, (1996) 531-44.

- 14-17 A. Nisati, *Muon rates at the LHC*, Proc. Large Hadron Collider workshop, Vol. II, eds. G. Jarlskog and D. Rein, CERN 90-10, ECFA 90-133, December 1990.
- 14-18 A. Fasso et al., *FLUKA: present status and future developments*, Proc. 4th International Conference on Calorimetry in High-energy Physics La Biodola, Elba, Italy; September 1993, edited by A. Menzione and A. Scribano.
- 14-19 *The ATLAS Technical Coordination Technical Design Report* (in preparation).
- 14-20 A. Nisati, *Fake level-1 muon-trigger rates in the ATLAS experiment*, ATLAS note DAQ-98-123, July 1998.
- 14-21 *The ATLAS Tile Calorimeter Technical Design Report*, CERN/LHCC/96-42, December 1996.